

# Multi-gigayear White Dwarf Cooling Delays from Clustering-enhanced Gravitational Sedimentation

Evan B. Bauer<sup>1</sup>, Josiah Schwab<sup>2,5</sup>, Lars Bildsten<sup>1,3</sup>, and Sihao Cheng (程思浩)<sup>4</sup>

Kavli Institute for Theoretical Physics, University of California, Santa Barbara, CA 93106, USA; ebauer@kitp.ucsb.edu

Department of Astronomy and Astrophysics, University of California, Santa Cruz, CA 95064, USA

Department of Physics, University of California, Santa Barbara, CA 93106, USA

Department of Physics and Astronomy, The Johns Hopkins University, Baltimore, MD 21218, USA

Received 2020 July 7; revised 2020 September 2; accepted 2020 September 3; published 2020 October 15

### **Abstract**

Cooling white dwarfs (WDs) can yield accurate ages when theoretical cooling models fully account for the physics of the dense plasma of WD interiors. We use MESA to investigate cooling models for a set of massive and ultramassive WDs (0.9–1.3  $M_{\odot}$ ) for which previous models have failed to match kinematic age indicators based on Gaia DR2. We find that the WDs in this population can be explained as C/O cores experiencing unexpectedly rapid <sup>22</sup>Ne sedimentation in the strongly liquid interior just prior to crystallization. We propose that this rapid sedimentation is due to the formation of solid clusters of <sup>22</sup>Ne in the liquid C/O background plasma. We show that these heavier solid clusters sink faster than individual <sup>22</sup>Ne ions and enhance the sedimentation heating rate enough to dramatically slow WD cooling. MESA models including our prescription for cluster formation and sedimentation experience cooling delays of  $\approx$ 4 Gyr on the WD Q branch, alleviating tension between cooling ages and kinematic ages. This same model then predicts cooling delays coinciding with crystallization of 6 Gyr or more in lower-mass WDs (0.6–0.8  $M_{\odot}$ ). Such delays are compatible with, and perhaps required by, observations of WD populations in the local 100 pc WD sample and the open cluster NGC 6791. These results motivate new investigations of the physics of strongly coupled C/O/Ne plasma mixtures in the strongly liquid state near crystallization and tests through comparisons with observed WD cooling.

Unified Astronomy Thesaurus concepts: White dwarf stars (1799); Stellar diffusion (1593); Cosmochronology (332)

### 1. Introduction

White dwarfs (WDs) are stellar embers that, when isolated from interaction with other stars, cool and fade over gigayear timescales as they radiate away their residual thermal energy and eventually crystallize (Fontaine et al. 2001; Althaus et al. 2010b). WD temperatures and luminosities therefore serve as important age indicators for these stars and their environments. Early work on WD cooling found that timescales for WD cooling depend primarily on thermal transport in the outer layers and the total thermal energy of the ionized plasma in the WD interior (Mestel 1952). Later work showed that as a WD becomes fainter and its interior cools, it is important to account for other sources of energy such as the latent heat released by interior phase transitions (van Horn 1968), chemical separation (Mochkovitch 1983; Isern et al. 1991; Segretain et al. 1994), and heavy element sedimentation (Bildsten & Hall 2001).

Recent data from the Gaia mission (Gaia Collaboration et al. 2016) have greatly enriched the sample of known WDs (Bergeron et al. 2019; Coutu et al. 2019; Kilic et al. 2020; McCleery et al. 2020) and enabled new tests of WD cooling theory and its applications. In particular, Cheng et al. (2019) recently studied a sample of nearby (within 250 pc), ultramassive WDs from the Gentile Fusillo et al. (2019) catalog, which is based on Gaia DR2 (Gaia Collaboration et al. 2018a, 2018b). Using the transverse velocity as a dynamical age indicator of this local population, they found evidence for a subpopulation of WDs that appear to be cooling much more slowly than predicted by WD cooling theory. Cheng et al.

(2019) estimated that this extra cooling delay may be explained by heat released as <sup>22</sup>Ne sediments in the WD interiors just before they crystallize. Our aim in this work is to investigate this claim using detailed evolutionary models of cooling WDs, and describe a physically motivated modification to the theory of <sup>22</sup>Ne sedimentation in WD interiors that can bring theoretical WD cooling models into agreement with observations.

The WDs that are the focus of the Cheng et al. (2019) study occupy a region of the HR diagram known as the WD "Q branch." This region is named for the DQ WDs showing spectral signatures of carbon in their atmospheres that are common in this region of the HR diagram and likely descend from WD mergers (Dunlap & Clemens 2015; Cheng et al. 2019; Coutu et al. 2019; Koester & Kepler 2019), though DA and DB WDs can also be found on the Q branch. The overdensity of massive and ultramassive WDs ( $M \approx 0.9$ –1.3  $M_{\odot}$ ) that forms the Q branch coincides with interior crystallization (Tremblay et al. 2019).

Cheng et al. (2019) argue based on transverse velocity data that 5%–10% of ultramassive WDs experience a cooling delay of 6–8 Gyr when they reach this region of the HR diagram. The total amount of energy available to be released by sedimentation of heavy elements (<sup>22</sup>Ne in particular) in the liquid interior prior to crystallization is enough to power a cooling delay of this magnitude (Bildsten & Hall 2001; Deloye & Bildsten 2002; García-Berro et al. 2008), but WD cooling and single-particle diffusion calculations indicate that these delays will not be realized unless the sedimentation rates are much higher than expected. We pursue the hypothesis that the necessary enhancement is caused by <sup>22</sup>Ne clustering and the subsequently more rapid sinking of larger clusters. While some previous WD

<sup>&</sup>lt;sup>5</sup> Hubble Fellow.

observations have set lower bounds on the order of 1 Gyr for the total cooling delays required from  $^{22}$ Ne sedimentation (e.g.,  $\approx 0.6\,M_{\odot}$  WDs in NGC 6791, Bedin et al. 2008; García-Berro et al. 2010), the 6–8 Gyr magnitude of the cooling delay for ultramassive WDs on the Q branch is by far the longest delay required by observational evidence. We therefore calibrate our  $^{22}$ Ne clustering model to satisfy the stringent requirements of the Q branch observations before going on to explore consequences for other WD populations.

In this work, we investigate detailed WD cooling models that account for these physical phenomena using the stellar evolution code Modules for Experiments in Stellar Astrophysics (MESA; Paxton et al. 2011, 2013, 2015, 2018, 2019). In Section 2, we describe how we use MESA to construct massive and ultramassive WD models suitable for cooling timescale calculations. Section 3 presents the physics of WD cooling and describes implementations in MESA, along with a set of standard MESA WD cooling models that provide a baseline expectation for cooling timescales in models that exclude <sup>22</sup>Ne sedimentation. In Section 4, we show that the diffusion coefficients for individual <sup>22</sup>Ne ions are now well constrained theoretically, and the resulting single-particle sedimentation speeds are too slow for the rate at which sedimentation energy must be released to explain the cooling delay for a subset of ultramassive WDs on the Q branch. Section 5 introduces MESA models implementing our proposed solution: an enhancement to sedimentation speeds due to the formation of heavier <sup>22</sup>Ne clusters in the strongly coupled liquid interior just before crystallization sets in. After calibrating our model to explain the observations of ultramassive WDs on the Q branch, we then explore predictions for cooling delays in lower-mass  $(0.6-0.8 M_{\odot})$  WDs. Appendices A-C provide further details on the physical formalism we employ for heating associated with mixing and sedimentation in multicomponent plasmas.

### 2. Initial WD Models

To construct massive and ultramassive C/O and O/Ne WD models, we begin from the input files of Lauffer et al. (2018) who previously created a suite of WD models with  $M \approx 1.0{-}1.3\,M_{\odot}$ . We use MESA version r10398 and make two important modifications to their approach. First, we use the nuclear network sagb\_NeNa\_MgAl.net. Unlike co\_burn\_plus.net used by Lauffer et al. (2018), this network includes <sup>23</sup>Na, which is produced in carbon burning and is typically the third most abundant isotope in an O/Ne WD (e.g., Siess 2006). Second, we turn off convective overshoot below the carbon burning flame, preventing the formation of hybrid CO/ONe WDs around  $\approx 1.1\,M_{\odot}$ .

We focus on WDs descended from metal-rich progenitors to maximize the potential effect of sedimentation heating on their cooling. We run a  $M_{\rm ZAMS} = 8.8~M_{\odot}$  model with initial metallicity of Z = 0.035, producing a  $0.98~M_{\odot}$  C/O WD. We also run a  $M_{\rm ZAMS} = 10~M_{\odot}$  model with metallicity Z = 0.035 that produces an O/Ne WD of mass  $1.06~M_{\odot}$ . We are particularly interested in studying long cooling delays due to sedimentation of <sup>22</sup>Ne, which appears in a WD interior at abundances that reflect the initial CNO abundances of the WD progenitor star. WDs that experience cooling delays of many gigayears from such a mechanism must descend from stars that formed in  $\alpha$ -element rich environments many gigayears ago. Fe abundances produced later in galactic chemical evolution are not relevant for the production of <sup>22</sup>Ne in WD interiors, so it is

likely that the most delayed WDs that we study here are related to the high  $[\alpha/\text{Fe}]$  population of old stars in the galactic disk (Nidever et al. 2014; Hayden et al. 2015; Mackereth et al. 2019; Sharma et al. 2020).

We also view our ultramassive C/O WD models as potentially representing WD merger products. The surface abundances of the R Coronae Borealis (RCB) stars, which are thought to be the products of He WD—C/O WD mergers. show evidence of nucleosynthesis that must occur in the aftermath of the merger (e.g., Jeffery et al. 2011). In particular, the extreme enhancement of <sup>18</sup>O observed in the RCB stars (Clayton et al. 2007) demonstrates the occurrence of CNOcycle hydrogen burning to produce  $^{14}$ N and the first steps of the helium-burning sequence  $^{14}$ N $(\alpha, \gamma)^{18}$ F $(e^+\nu)^{18}$ O $(\alpha, \gamma)^{22}$ Ne that, if completed, would produce <sup>22</sup>Ne. Calculations in the RCB context (e.g., Staff et al. 2012) indicate that mergers could plausibly lead to enhancements in the <sup>22</sup>Ne mass fraction of  $\approx 0.05$  in the  $\approx 0.1 \, M_{\odot}$  hot, dense region created around the interface of the merged WDs. While locally significant, when distributed across the WD, this amount of <sup>22</sup>Ne would represent an enrichment to the <sup>22</sup>Ne mass fraction of 0.01 or less, so the merger process appears likely to provide at most a modest enhancement to  $^{22}{\rm Ne.}$  Broadly, we view our ultramassive C/O WD models as representing double C/O WD merger products, in which each WD individually processed its initial CNO metallicity into <sup>22</sup>Ne, the merger process itself produced negligible further enrichment of <sup>22</sup>Ne, and so the <sup>22</sup>Ne abundance throughout the bulk of the final WD merger product still approximately reflects the initial metallicity with which the stars were formed.

The Lauffer et al. (2018) models completely remove the stellar envelope with strong winds. This choice is not physically motivated, but allows the models to skip the challenging and time-consuming evolution through the thermally pulsing asymptotic giant branch (TP-AGB). As a result, the outer layers of the WD that are assembled during the TP-AGB and the final H and He layers are not self-consistently generated in our models. To create a simple He atmosphere, we then add  $10^{-3}\,M_\odot$  of pure He by accretion on the surface before cooling begins. Subsequent diffusion at the boundary between this outer He layer and the underlying C quickly establishes a smooth transition region at the base of the He envelope.

As DB WDs, our models will not always match the spectral classification of the many DQ and DA WDs found in the Q branch region of the color–magnitude diagram (CMD), but their cooling properties will be sufficient for our study here. Ultramassive WDs on the Q branch are still relatively luminous and hot, and so the cooling timescales of DA and DB WDs in this regime are very similar (Camisassa et al. 2019). Only after cooling below the Q branch do DA and DB WDs develop significantly different cooling timescales. Similarly, we expect that DQ WDs do not have markedly different cooling properties from DB WDs on the Q branch, though we are not aware of any detailed studies that model DQ WD cooling timescales specifically.

In order to study the range of WD masses relevant for the Q branch (0.9–1.3  $M_{\odot}$ ), we scale the mass of these models using the MESA control <code>relax\_mass\_scale</code>. This preserves the composition profile as a function of fractional mass coordinate. As a consequence, our models cannot explore the effects of any mass-dependent trends in the chemical composition, but this is not important for our purposes. This scaling procedure allows

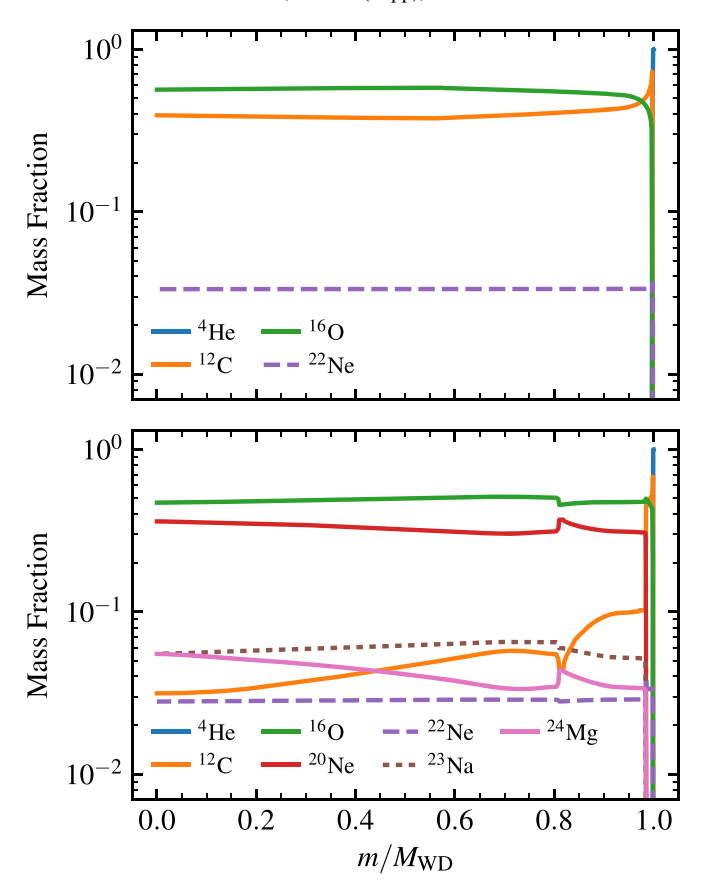


**Figure 1.** Composition profiles of our initial WD models descended from Z=0.035 progenitors. The top panel shows our C/O WD model and the bottom panel shows our O/Ne WD model.

us to easily construct models that are difficult to produce from single star evolution, such as C/O WDs with  $M\gtrsim 1.05\,M_\odot$  created by WD mergers.

Figure 1 shows the initial composition profiles of our WD models. Our C/O WD model can be compared with composition profiles from other evolutionary calculations forming massive C/O WDs (e.g., Althaus et al. 2010a; Romero et al. 2013) and has similar <sup>12</sup>C and <sup>16</sup>O abundances in the core. Our O/Ne WD model can be compared with the composition profiles from the ultramassive WDs of Camisassa et al. (2019). The mass fractions of <sup>12</sup>C, <sup>16</sup>O, <sup>20</sup>Ne, <sup>23</sup>Na, and <sup>24</sup>Mg are all comparable, while our models have more <sup>22</sup>Ne given their higher metallicity. This demonstrates that our more approximate evolutionary approach provides composition profiles representative of state-of-the-art WD models.

# 3. Cooling Models

The model construction process yields WDs for which nuclear reactions have ceased. They have core temperatures of  $T_{\rm c}\approx 10^8$  K and effective temperatures of  $T_{\rm eff}\approx 10^5$  K. We run WD cooling calculations based on these models using MESA r12115. Figure 2 shows cooling tracks for massive and ultramassive C/O WD models on the Gaia CMD in the region of the Q branch. The colors for these tracks on the Gaia CMD are interpolated based on  $\log g$  and  $T_{\rm eff}$  from the MESA tracks using the Montreal synthetic color tables for DB WDs (Holberg & Bergeron 2006; Bergeron et al. 2011; Blouin et al. 2018).

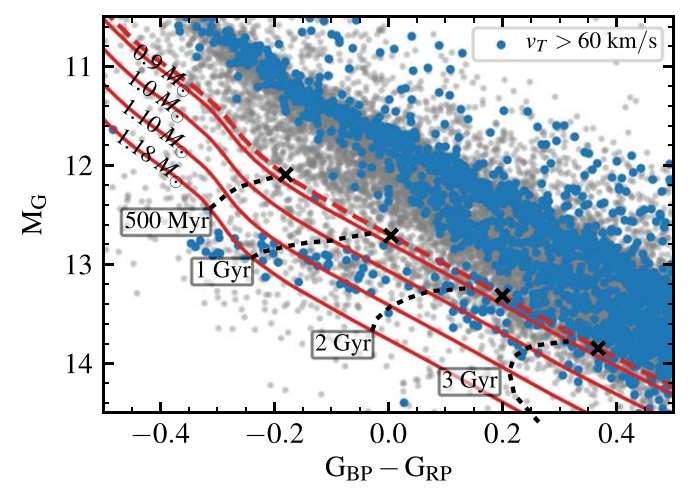


Figure 2. C/O WD cooling tracks (red lines) on the Gaia CMD in the region of massive and ultramassive WDs on the Q branch (the mostly horizontal feature in the data around  $M_G \approx 13$ ). Black-dashed curves represent contours of constant WD cooling age (not including prior main sequence lifetime) for WDs that experience no delay due to heavy element sedimentation. The red-dashed line shows a Montreal cooling track for a 0.9  $M_{\odot}$  DB WD, and black x's mark ages along that track for comparison to the age contours of our MESA WD models. Gray points represent WDs within 150 pc according to Gaia, while blue points represent those WDs for which Gaia proper motion measurements also imply velocities transverse to our line of sight  $v_T > 60$  km s<sup>-1</sup>.

The coverage of these tables places an upper limit on the accessible mass range for Gaia colors around 1.2  $M_{\odot}$ . We can run MESA models more massive than this without difficulty if no colors are needed, but this mass range will be sufficient for our analysis in this work.

The WD data and kinematics in Figure 2 are based on Gaia DR2 (Gaia Collaboration et al. 2018a, 2018b) with quality cuts of Cheng et al. (2019) and limited to a distance of 150 pc. Cheng et al. (2019) have argued that the transverse velocity ( $\nu_T$ ) data from Gaia provide an independent dynamical indicator of the WD ages, and that there is evidence of a kinematically old population (represented here by  $\nu_T \gtrsim 60~{\rm km~s^{-1}}$ ) that must experience a cooling delay of several gigayears in the region of the Q branch. This is clearly inconsistent with the much faster cooling rates exhibited by the tracks in Figure 2, and this motivates deeper exploration of the physical processes that may modify cooling rates in this regime.

Our models have pure He atmospheres, so we employ a set of atmospheric boundary conditions for DB WDs based on the Koester (2010) WD atmosphere code (O. Toloza 2019, private communication). These tables are important when WDs cool to  $T_{\rm eff} < 15{,}000~{\rm K}$  and the conditions for the cool, dense He at the photosphere run off the MESA opacity tables as He becomes neutral. These boundary conditions tabulate pressure and temperature at an optical depth of  $\tau = 25~{\rm where}~{\rm MESA}$  can attach an interior profile using its gray opacity tables, similar to what is described for DA WDs in Paxton et al. (2013) based on the H atmosphere models of Rohrmann et al. (2012). The tabulated atmospheres for DB WDs are publicly available as a standard atmosphere option in MESA r12115.

Crystallization in WD interiors releases latent heat that slows WD cooling by up to  $\approx 1$  Gyr (van Horn 1968; Lamb & van Horn 1975; Chabrier et al. 2000; Fontaine et al. 2001), and Tremblay et al. (2019) demonstrated that crystallization in their C/O WD models coincides with the Q branch region on the CMD. Pileup during crystallization can explain some of the overdensity of objects that forms the Q branch, but Tremblay

<sup>6</sup> http://www.astro.umontreal.ca/~bergeron/CoolingModels/

et al. (2019) showed that this overdensity is even more strongly peaked than expected from latent heat release alone. The several gigayear cooling delay inferred by Cheng et al. (2019) for kinematically old objects (blue points in Figure 2) on the  $\mathcal{Q}$  branch is a delay with respect to models that already include latent heat release upon crystallization.

The cooling models in Figure 2 include the latent heat released by crystallization, but neglect any heating due to sedimentation of heavy elements, corresponding to the case of WDs descended from low-metallicity progenitors. Figure 2 also includes a track for a 0.9  $M_{\odot}$  DB WD from the Montreal WD cooling models (Fontaine et al. 2001). This track appears slightly offset from the MESA model of the same mass because the Montreal models use a 50/50 C/O core composition by mass fraction, while the ashes of He burning in our MESA models leave behind a core composition that is closer to 60% oxygen by mass, resulting in slightly more compact C/O WD cores. The Montreal models do not include any heavy element sedimentation in the interior, and the cooling timescales for the Montreal model agree well with the MESA models that do not include sedimentation heating.

### 3.1. Crystallization

The onset of crystallization can be quantified using the average Coulomb coupling parameter of ions in the WD interior plasma:

$$\Gamma \equiv \frac{\langle Z_{\rm i}^{5/3} \rangle e^2}{a_c k_{\rm B} T},\tag{1}$$

where  $a_{\rm e} \equiv (3/4\pi n_{\rm e})^{1/3}$  is the electron separation and  $Z_{\rm i}$  is the ion charge. The plasma is strongly coupled for  $\Gamma \geqslant 1$ , and a classical one-component plasma (OCP) experiences a phase transition from liquid to solid for  $\Gamma = 175$  (Potekhin & Chabrier 2010). In a WD interior,  $\Gamma$  increases as the WD cools, and crystallization begins in the center when  $\Gamma$  passes a critical threshold  $\Gamma_{crit}$ . For a WD interior composed of a single species of ions (e.g., pure C or pure O), this critical value for crystallization matches the OCP value ( $\Gamma_{crit} = 175$ ), but for plasma mixtures the phase curve is more complex (Horowitz et al. 2010; Medin & Cumming 2010; Blouin et al. 2020). For the mixtures dominated by two elements such as C/O or O/Ne characterizing WD interiors, the presence of trace impurities such as <sup>22</sup>Ne does not appear to have a significant impact on the overall phase curve, which can be adequately described by calculations for two-component mixtures (Hughto et al. 2012). For mixtures such as C/O or O/Ne, we approximate the results of Medin & Cumming (2010) and Blouin et al. (2020) by adopting a crystallization temperature that is the critical temperature of a plasma composed purely of the lighter element of the mixture. That is, crystallization occurs for

$$\Gamma = \frac{\langle Z_{\rm i}^{5/3} \rangle e^2}{a_{\rm e} k_{\rm B} T} > \Gamma_{\rm crit} = 175 \frac{\langle Z_{\rm i}^{5/3} \rangle}{Z_{\rm light}^{5/3}}.$$
 (2)

This approximation agrees with Medin & Cumming (2010) to within about 5% for mixtures where the heavier element is not too abundant by number fraction:  $Y_{\text{heavy}} \lesssim 0.5$ , which is valid for the C/O and O/Ne dominated interiors of the WD models in this work. Equation (2) gives  $\Gamma_{\text{crit}} \approx 230$  for C/O mixtures and  $\Gamma_{\text{crit}} \approx 210$  for O/Ne mixtures.

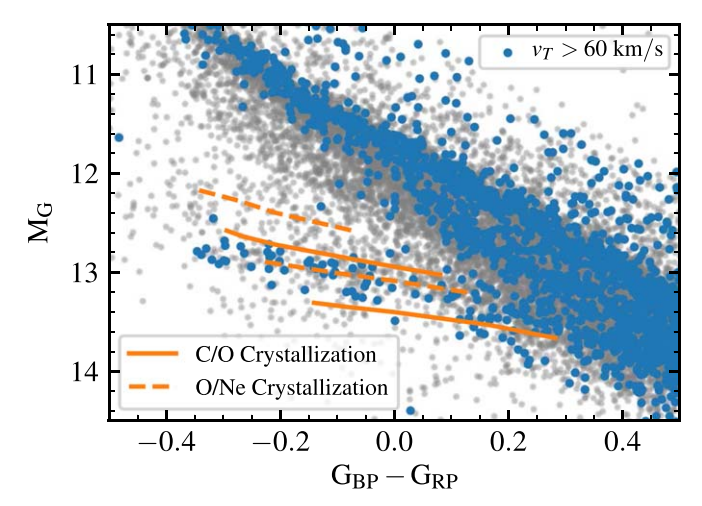


**Figure 3.** Crystallization in ultramassive O/Ne and C/O WD models compared to the Gaia WD sample within 150 pc. Contours are for cooling models of  $M=0.9-1.18~M_{\odot}$ , with the upper contour corresponding to the location where 20% (by mass) of the interior has crystallized and the lower contour where 80% has crystallized, as in Tremblay et al. (2019).

Our MESA models do not include phase separation of C/O upon crystallization, which may provide an additional delay of up to 1 Gyr coinciding with crystallization (Mochkovitch 1983; Segretain & Chabrier 1993; Segretain et al. 1994; Chabrier et al. 2000; Althaus et al. 2012). However, the magnitude of this delay is much smaller than the several gigayear delay on the Q branch required by the analysis of Cheng et al. (2019), and we do not expect phase separation to change the location of crystallization on the CMD significantly. For simplicity, we therefore ignore phase separation in our models for this work.

The MESA treatment of crystallization in WDs employs the Potekhin & Chabrier (2010) equation of state (EOS) and allows  $\Gamma_{\rm crit}$  to be set as a user-defined parameter (Paxton et al. 2018), so our WD models set this parameter according to Equation (2). Due to the higher average charge of ions in O/Ne WDs, Equations (1) and (2) predict that they will crystallize at interior temperatures that are  $\approx 50\%$ -60% higher than C/O WDs of the same density. Figure 3 shows that this difference translates into a significant offset on the CMD between O/Ne and C/O crystallization sequences for ultramassive WDs. The contours in Figure 3 rely on a grid of MESA WD cooling models with  $M = 0.9-1.18 M_{\odot}$ . These models have helium atmospheres and include crystallization and latent heat release as part of the evolution. Hydrogen atmospheres change the colors somewhat for any given model, but the overall location of the crystallization contours does not change much for different atmosphere compositions.

The location of the Q branch WD overdensity on the CMD is inconsistent with O/Ne crystallization, but is consistent with C/O cores even for WDs with mass  $M > 1.05 M_{\odot}$ . Furthermore, the delays due to sedimentation heating that will be discussed in subsequent sections require that the WD interior remain liquid in order for diffusion to be active. After crystallization, no further sedimentation heating is possible, and the cooling cannot be slowed to form an overdensity of kinematically old WDs on the CMD. The kinematics and current CMD positions of WDs in Figure 3 require that most of the several gigayear cooling delay inferred by Cheng et al. (2019) occurs after reaching cooler temperatures than allowed by O/Ne crystallization if heavy element sedimentation is the

cause. Only the C/O crystallization sequence is consistent with the location of the *Q* branch CMD overdensity.

These WDs on the O branch with  $M > 1.05 M_{\odot}$  and C/O cores may be the products of C/O WD mergers that avoid core C ignition during the merger process. Using velocities of WDs above the Q branch, Cheng et al. (2019, 2020) estimated that about 30% of WDs in this mass range originate from WD mergers, in line with recent binary population synthesis predictions of Temmink et al. (2020). Kilic et al. (2020) reached a similar conclusion for massive WDs in their sample of spectroscopically confirmed DA WDs within 100 pc in the Sloan Digital Sky Survey footprint. Indeed, Dunlap & Clemens (2015) have also argued that ultramassive DQ WDs are likely WD merger products, and Coutu et al. (2019) and Cheng et al. (2019) recently found that about 45% of ultramassive DQ WDs, a significant fraction of WDs on the Q branch, are kinematically old, thus indicating a clear relationship between WD mergers and the cooling delay.

If WD mergers are the only way to produce C/O WDs in this mass range, Figure 3 clearly suggests that a high merger fraction among this ultramassive WD population is needed to produce the overdensity of WDs on the CMD aligned with C/O crystallization, which is then further accentuated by the cooling delay that some C/O WDs on the Q branch experience. There is no apparent CMD overdensity of WDs corresponding to O/Ne crystallization, which limits the fraction of WDs in this mass range produced by single-star evolution or any cooling delay they might experience associated with O/Ne crystallization. As we are primarily seeking to explain the cooling delay for the kinematically old WDs (blue points) that sit in the C/O crystallization regime in Figure 3, we shall proceed with C/O cooling models for much of the remainder of this work, even for masses well above  $1.0 \ M_{\odot}$ .

## 4. Single-particle Sedimentation Heating

Diffusion and sedimentation of ions in WD interiors can rearrange the charge and mass distribution, releasing heat that slows the rate of WD cooling (Isern et al. 1991; Bildsten & Hall 2001; Deloye & Bildsten 2002; García-Berro et al. 2008). In this section, we argue that cooling delays comparable to the several gigayears inferred by Cheng et al. (2019) can be explained by sedimentation of <sup>22</sup>Ne, but only if it occurs much faster than predicted by single-particle diffusion calculations. While the total energy available from this sedimentation is more than sufficient to provide the observed cooling delay, the required speed is large compared to expectations for <sup>22</sup>Ne diffusive sedimentation based on single-particle diffusion coefficients. Therefore, we will consider the possibility of <sup>22</sup>Ne cluster formation that substantially enhances the sedimentation rate.

### 4.1. Sedimentation of Neutron-rich Isotopes

In degenerate WD interiors, the electric field balances the gravitational force acting on the ions of average charge-to-mass ratio (Bildsten & Hall 2001; Chang et al. 2010):

$$eE = \frac{\langle A \rangle}{\langle Z_i \rangle} m_p g \approx 2 m_p g. \tag{3}$$

The net gravitational sedimentation force on ions of species j is therefore

$$F_{g,j} \equiv -A_j m_p g + Z_j e E = -\left(A_j - Z_j \frac{\langle A \rangle}{\langle Z_i \rangle}\right) m_p g.$$
 (4)

The quantity  $A_j - Z_j \langle A \rangle / \langle Z_i \rangle$  is the number of extra neutrons of an isotope relative to ions of average charge-to-mass ratio in the background plasma. This term is large for neutron-rich isotopes, such as <sup>22</sup>Ne found in C/O WD interiors, and both <sup>22</sup>Ne and <sup>23</sup>Na in O/Ne WD interiors.

For stars massive enough to burn hydrogen through the CNO cycle, this process converts the primordial CNO abundance into  $^{14}N$ , which then undergoes the  $\alpha$ -capture sequence  $^{14}N(\alpha, \gamma)^{18}F(e^+\nu)^{18}O(\alpha, \gamma)^{22}Ne$  during He-burning stages. Therefore most of the initial metallicity Z of these stars will become <sup>22</sup>Ne distributed evenly through the interior profile of C/O or O/Ne WDs. In addition, more massive stars that ignite interior carbon burning on the AGB before shedding their envelopes to become O/Ne WDs also produce a significant amount of  $^{23}$ Na. This occurs as a result of the  $^{12}$ C +  $^{12}$ C reaction that branches to  $^{23}$ Na + p with  $\approx$ 50% probability. The overall neutron content of the mixture is enhanced through subsequent captures of the proton and electron capture or positron emission by those products. Importantly, these <sup>12</sup>C burning products are metallicity independent and so <sup>23</sup>Na is generically present in the interior profile of O/Ne WDs at a mass fraction of  $X_{\text{Na}} \approx 0.05$  (e.g., Siess 2006, 2007).

The WD cooling delay caused by a total energy  $\mathcal{E}$  released at WD luminosity  $L_{\rm WD}$  is  $t_{\rm delay} \sim \mathcal{E}/L_{\rm WD}$ . We will describe these energies in terms of the potential energy change associated with particles of species j in the plasma traveling a distance  $R_{\rm WD}$  under the influence of force  $F_j$ :  $\mathcal{E} \sim |F_j|R_{\rm WD}X_jM_{\rm WD}/A_jm_{\rm p}$ , where  $X_j$  is the mass fraction of element j and  $A_j$  is its atomic mass number. Taking a luminosity of  $L_{\rm WD} \approx 10^{-3}\,L_{\odot}$  as representative of WDs on the Q branch, and  $g \approx 10^9\,{\rm cm~s^{-2}}$  as the typical local gravity in the interior of a 1  $M_{\odot}$  WD, we can express the upper limit for the total time delay as

$$t_{\text{max}} \approx 10 \text{ Gyr} \left( \frac{X_j/A_j}{10^{-3}} \right) \left( \frac{|F_j|}{m_p g} \right)$$
$$\times \left( \frac{g}{10^9 \text{ cm s}^{-2}} \right) \left( \frac{10^{-3} L_{\odot}}{L_{\text{WD}}} \right) \left( \frac{R_{\text{WD}}}{10^{-2} R_{\odot}} \right) \left( \frac{M_{\text{WD}}}{M_{\odot}} \right). \tag{5}$$

This represents the total available time delay from a given energy source as it requires all of the element in question to move through the entire potential of the star. The maximum time delay predicted by Equation (5) for  $^{22}$ Ne sedimentation is  $\approx (10 \text{ Gyr})(Z/0.01)$ , while  $^{23}$ Na could provide an additional delay up to  $\approx 25 \text{ Gyr}$ .

Another potential driver of sedimentation and heating in WD interiors is charge stratification in strongly coupled plasma, the ion chemical potentials pushing ions of higher charge toward the center even for ions of average charge-to-mass ratio (Chang et al. 2010; Beznogov & Yakovlev 2013). In Appendix C we use Equation (5) to show that additional heating associated with this physics is negligible compared to sedimentation driven by the weight of neutron-rich isotopes, so we ignore any additional sedimentation heating from charge stratification for our models in this paper.

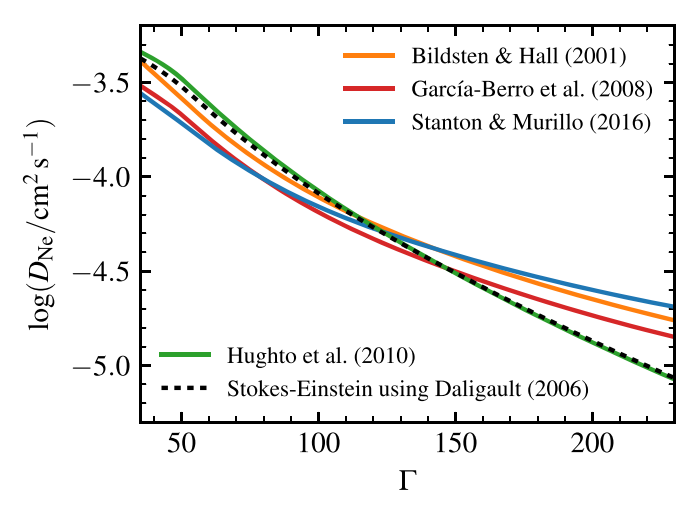


Figure 4. Comparison of single-particle diffusion coefficients in the interior of a MESA C/O WD model near crystallization.

While Equation (5) quantifies the maximum delay available from sedimentation energy, accurate prediction of the total time delay achieved from diffusive sedimentation requires detailed models of WD cooling and interior diffusion (Bildsten & Hall 2001; Deloye & Bildsten 2002; García-Berro et al. 2008).

# 4.2. Single-particle Diffusion Coefficients

The rate at which  $^{22}$ Ne sedimentation deposits heat in the interior depends directly on the diffusion velocity of  $^{22}$ Ne:  $\epsilon_{22} \propto \nu_{\text{Ne}}$  (see Equation (12) and Appendix B). For trace  $^{22}$ Ne sinking in the WD interior, this velocity is

$$v_{\text{Ne}} = 2m_{\text{p}}g \frac{D_{\text{Ne}}}{k_{\text{B}}T},\tag{6}$$

and so  $\epsilon_{22} \propto D_{\rm Ne}$ , where  $D_{\rm Ne}$  is the single-particle <sup>22</sup>Ne diffusion coefficient. Uncertainties in the value of this coefficient at strong ion coupling ( $\Gamma \gtrsim 10$ ) have been a source of uncertainty regarding the total rate of <sup>22</sup>Ne heating in past studies (Bildsten & Hall 2001; Deloye & Bildsten 2002; García-Berro et al. 2008).

Recent calculations of  $D_{\rm Ne}$  in the strongly coupled regime of C/O WD interiors have reduced the current uncertainty to no more than a factor of 2, and likely substantially smaller. Hughto et al. (2010) performed molecular dynamics (MD) simulations of C/O plasma mixtures with trace  $^{22}$ Ne characteristic of WD interiors over a plasma coupling range including strongly liquid conditions  $1 < \Gamma < 244$ . They calculated  $D_{\rm Ne}$  based on these simulations by measuring the velocity autocorrelation functions for  $^{22}$ Ne particles and provided a fitting formula for  $D_{\rm Ne}$ . Figure 4 shows  $D_{\rm Ne}$  using the Hughto et al. (2010) fitting formula in the interior profile of a MESA C/O WD model for which crystallization has just begun near the center ( $\Gamma_{\rm center} = 237$ ). The figure also shows  $D_{\rm Ne}$  calculated for the same MESA WD profile using the methods of two previous studies of  $^{22}$ Ne sedimentation in WDs (Bildsten & Hall 2001; García-Berro et al. 2008), demonstrating agreement within a factor of 2 throughout most of the WD interior profile.

Figure 4 also shows  $D_{\rm Ne}$  based on the coefficients calculated by Stanton & Murillo (2016), which are the default diffusion coefficients in MESA. This formalism calculates diffusion coefficients based on binary collision integrals between each pair of species in the plasma. In the limit of a trace (Ne)

sedimenting through a fixed background (C and O), the total diffusion coefficient can be expressed in terms of a sum over the binary resistance coefficients  $K_{ij}$  used in the Burgers (1969) diffusion formalism as

$$D_{\text{Ne,SM}} = \frac{n_{\text{Ne}} k_{\text{B}} T}{\sum_{i} K_{i,\text{Ne}}} \approx \frac{n_{\text{Ne}} k_{\text{B}} T}{K_{\text{O,Ne}} + K_{\text{C,Ne}}},\tag{7}$$

where the sum can be reduced to just the terms for C and O as these form the dominant background in which most collisions that mediate diffusion occur.

Finally, Bildsten & Hall (2001) noted that in the liquid regime, an estimate of the single-particle effective radius *R* yields the Stokes–Einstein diffusion coefficient:

$$D = \frac{k_{\rm B}T}{4\pi\eta R},\tag{8}$$

where  $\eta$  is the viscosity of the liquid. Using MD simulations of an OCP, Daligault (2006a) showed that in the strongly liquid regime ( $\Gamma \gtrsim 30$ ) Equation (8) surprisingly holds even for an individual ion when the radius is taken to be  $R=0.73a_{\rm i}$ , where  $a_{\rm i}=(3/4\pi n_{\rm i})^{1/3}$  is the ion spacing. It is straightforward to generalize this result to estimate a Stokes–Einstein diffusion coefficient for ions in a plasma mixture. Daligault (2006a) gave the following fit based on MD for the viscosity of the OCP in the strongly liquid regime:

$$\eta = 0.10 m_{\rm i} n_{\rm i} a_{\rm i}^2 \omega_{\rm p} e^{0.008\Gamma},\tag{9}$$

where  $m_i$  is the mass of the ions in the OCP, and  $\omega_p$  is the plasma frequency defined below. In order the extend this to an average over ions in a mixture, we use  $\Gamma$  as defined for a mixture in Equation (1), along with  $m_i = \langle A \rangle m_p$  and

$$\omega_{\rm p} = \left(\frac{4\pi n_{\rm i} \langle Z_{\rm i}^2 \rangle e^2}{\langle A \rangle m_{\rm p}}\right)^{1/2}.\tag{10}$$

For a mixture, the ion density is  $n_i = \rho/\langle A \rangle m_p$ , and the electron density satisfies  $n_e = \langle Z_i \rangle n_i$ . For an ion species of charge  $Z_j$  different from the background  $\langle Z_i \rangle$ , we rescale the effective radius for Stokes–Einstein drift to account for the different size of its charge-neutral sphere in a background of fixed electron density  $n_e$ , with the result

$$R_j = 0.73a_i \left(\frac{Z_j}{\langle Z_i \rangle}\right)^{1/3}.$$
 (11)

For  $^{22}$ Ne in a C/O background  $R_{\text{Ne}} = 0.82a_{\text{i}}$ , and the black-dashed curve in Figure 4 shows the resulting diffusion coefficient when using this radius along with Equation (8).

Figure 4 demonstrates that although Hughto et al. (2010) make no mention of Stokes–Einstein diffusion in relation to their MD simulations for C/O/Ne mixtures, their fits for diffusion coefficients closely match the Stokes–Einstein prediction in the liquid regime when using a radius scaled to the OCP results of Daligault (2006a). The Stokes–Einstein scaling for diffusion coefficients holds throughout the liquid WD interior, and so we will continue to make use of the prediction of Equation (8) in later sections whenever a coefficient is needed for particles where the size R can be calculated.

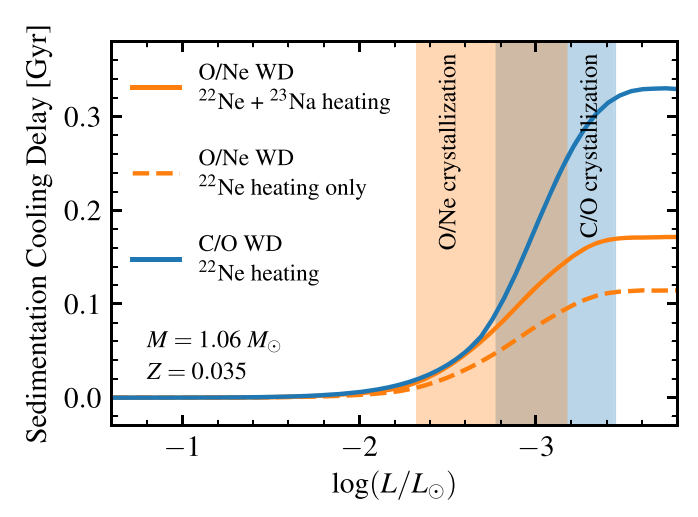


Figure 5. Accumulated cooling delays due to single-particle sedimentation heating relative to models that include no sedimentation heating for 1.06  $M_{\odot}$  WD models descended from metal-rich progenitors (Z=0.035). The orange curves show cooling delays for WDs with O/Ne cores, while the blue curve shows the cooling delay for a C/O WD. The shaded regions indicate the luminosity range over which the model interiors pass from 10% crystallized to 90% crystallized for O/Ne (orange) and C/O (blue) WD cores.

As a baseline for Ne diffusion in liquid WD interiors, we adopt the coefficient fitting formula of Hughto et al. (2010). In practice, we implement this by rescaling the Ne diffusion velocity in the MESA model by a factor of  $D_{\rm Ne, Hughto}/D_{\rm Ne, SM}$ , with a smooth transition from the default diffusion based on Stanton & Murillo (2016) over the range  $30 < \Gamma < 50$ , where this results in a modest enhancement to the diffusion speed (less than a factor of 2).

# 4.3. Implementation of Sedimentation in MESA

The implementation of element diffusion in MESA is described in Section 3 of Paxton et al. (2018), including the addition of a sedimentation heating source term. In Paxton et al. (2018), this term included only <sup>22</sup>Ne (which is typically dominant) but here we modify MESA to include heating associated with the diffusion of all isotopes included in the nuclear network. This allows inclusion of <sup>23</sup>Na sedimentation, which is of comparable importance in O/Ne WDs. The generalized heating term in MESA is implemented as a local entropy source

$$\epsilon_{\text{diff}} = \sum_{\text{ions}} (A_j m_p \mathbf{g} + Z_j e \mathbf{E}) \cdot \frac{X_j \mathbf{v}_{\text{diff},j}}{A_j m_p}, \tag{12}$$

where  $X_j$  is the mass fraction of ion species j, and  $v_{\text{diff},j}$  is the local diffusion velocity found by the diffusion solver along with the electric field E. Refer to Appendix B.2.2 for the formal justification for this form of the heating term, which is a slightly simplified version of Equation (B14). For most C/O WDs, Equation (12) is dominated by the <sup>22</sup>Ne contribution and reduces to the form found in Equation (16) of Paxton et al. (2018). A more complete physical description of the heating associated with chemical transport in multicomponent plasmas is given in Appendices A and B.

Figure 5 shows cooling delays due to this single-particle sedimentation heating for 1.06  $M_{\odot}$  MESA WD models (both O/ Ne and C/O). With the diffusion velocities calculated for single particles, the neutron-rich isotopes sediment toward the center very slowly, releasing only a small fraction of the potential heating available according to Equation (5) before crystallization sets in and halts sedimentation. Orange curves in Figure 5 show two cases for the same O/Ne WD model: one for which we include all sedimentation heating according to Equation (12) (most importantly <sup>22</sup>Ne and <sup>23</sup>Na), and one for which we only include the <sup>22</sup>Ne sedimentation heating. While the inclusion of <sup>23</sup>Na heating does enhance the overall cooling delay for the O/Ne model, it still provides a much shorter delay than the C/O model of the same mass experiences from <sup>22</sup>Ne alone (blue curve) due to faster diffusion of heavy elements in a C/O background than an O/Ne background. For the C/O case, crystallization (indicated by the shaded regions) also occurs later, prolonging the sedimentation period and further enhancing the cooling delay. The C/O WD model uses the <sup>22</sup>Ne diffusion coefficients based on Hughto et al. (2010), while the O/Ne model employs the default MESA diffusion coefficients of Stanton & Murillo (2016) because we have no MD results for this case. Even though Figure 4 indicates that the Stanton & Murillo (2016) coefficients are likely too high in the strongly liquid regime, these O/Ne models still have significantly shorter cooling delays than the C/O model. It would also be possible to compute the Stokes-Einstein diffusion coefficients of Equations (8)–(11) for the O/Ne case, but this would only result in slower diffusion and a smaller cooling delay.

None of these cases using single-particle diffusion coefficients experience diffusion that is fast enough to provide heating adequate to create the several gigayear cooling delay required by Cheng et al. (2019). Figure 6 shows interior heating profiles from single-particle <sup>22</sup>Ne sedimentation in the interior of our 1.06  $M_{\odot}$  C/O WD model. In order to verify that our heating term in MESA matches expectations, we compare to a semi-analytic estimate that relies only on the basic thermodynamic structure of the MESA model ( $\Gamma$ , T,  $X_i$ ), approximating Equation (12) as

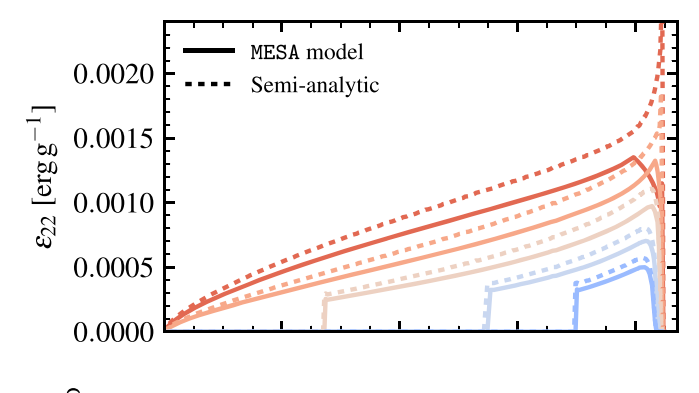
$$\epsilon_{22} = 2m_{\rm p}g \frac{X_{\rm Ne} \nu_{\rm Ne}}{22m_{\rm p}},$$
(13)

with  $v_{\text{Ne}}$  given by Equation (6) and the diffusion coefficient  $D_{\text{Ne}}$  given by the fit of Hughto et al. (2010). The total integrated <sup>22</sup>Ne sedimentation luminosity never exceeds 20% of the total WD luminosity, and so this model with single-particle sedimentation speeds cannot significantly slow the WD cooling to achieve a multi-gigayear delay.

### 5. Clustering

While the energy available from  $^{22}$ Ne sedimentation is clearly adequate to provide the necessary cooling delay observed for Q branch WDs, this sedimentation must occur significantly faster than predicted by single-particle diffusion coefficient calculations. Motivated by this as well as the fact that the cooling delay clearly coincides with approaching interior crystallization, we hypothesize that clusters of  $^{22}$ Ne form in the strongly liquid regime near crystallization. In this regime, neighboring particles become associated with each other for many plasma oscillation timescales (Donkó et al. 2002), and heavy elements may therefore form clusters that

<sup>&</sup>lt;sup>7</sup> The implementation of sedimentation in MESA differs from the approach taken by García-Berro et al. (2008). In Appendix B, we clarify the difference between these treatments and show that the net energetics are equivalent.



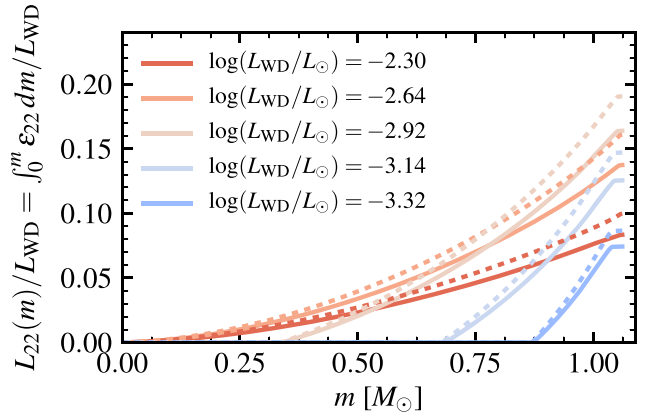


**Figure 6.** <sup>22</sup>Ne heating and integrated luminosity profiles for a 1.06  $M_{\odot}$  C/O WD descended from a Z=0.035 progenitor. The dashed curves show the semi-analytic heating estimate described in the text, while the solid curves are the heating profiles from the MESA model including the full diffusion solution.

behave as larger particles even as the background remains liquid, enhancing the rate of diffusion (Medin & Cumming 2011). These clusters will, as we show, sink faster.

The pressure gradient responsible for maintaining hydrostatic equilibrium in the degenerate WD interior depends primarily on the electron density  $n_{\rm e}$ , so we demand that  $n_{\rm e}$  remain constant for local variations in ion composition. In this case, a cluster of particles composed purely of species j will have a Coulomb coupling parameter of

$$\Gamma_j = \frac{Z_j^{5/3}}{\langle Z_i^{5/3} \rangle} \Gamma. \tag{14}$$

For Ne in a C/O background, this gives  $\Gamma_{Ne} \approx 1.8\Gamma$ . Hence, a group of Ne particles is much more strongly coupled than the surrounding ions, and may begin to form solid clusters when the background C/O reaches strongly liquid conditions. Even if only a fixed cluster for a finite time, a solid cluster will diffuse and sediment through the still liquid background as a heavier single particle. For specific conditions, we expect clusters to have a distribution of sizes. We use  $\langle N \rangle$  to represent the number of Ne atoms in an average-size cluster. Cluster nucleation has been studied for a liquid OCP near crystallization (Daligault 2006b; Cooper & Bildsten 2008), but it is not immediately clear how to extend this work to mixtures of different particle charges, so we leave  $\langle N \rangle$  as a free parameter for our exploratory modeling in this work. Maintaining the same electron density  $n_e$  as the surrounding plasma, the radius

for a cluster containing  $\langle N \rangle$  particles is

$$R_{\text{cl},j} = a_{i} \left( \frac{\langle N \rangle Z_{j}}{\langle Z_{i} \rangle} \right)^{1/3}.$$
 (15)

The total downward sedimentation force on a cluster of  $\langle N \rangle$  <sup>22</sup>Ne particles is  $2m_p g \langle N \rangle$ , so Stokes–Einstein drift in the liquid regime predicts that the velocity of cluster sedimentation is

$$v_{\rm cl} = 2m_{\rm p}g\langle N \rangle \frac{D_{\rm cl}}{k_{\rm B}T}.$$
 (16)

The diffusion coefficient  $D_{\rm cl}$  can be obtained from Equation (8) using the radius of Equation (15). Since we have shown that individual ions diffuse as spheres of radius given by Equation (11) following Stokes–Einstein drift, we express the cluster diffusion velocity in terms of a simple rescaling of the individual particle velocities to larger, heavier clusters diffusing in a background plasma of the same viscosity. By comparison with Equation (6), we can write the diffusion velocity of a cluster of Ne particles in terms of the diffusion velocity for individual Ne ions as

$$v_{\rm cl} = 0.73 \langle N \rangle^{2/3} v_{\rm Ne}.$$
 (17)

Note that this expression assumes that the diffusion velocity is dominated by drift due to external forces (gravity and the electric field) and ignores "ordinary diffusion" due to composition gradients. This is justified in strongly degenerate WD interiors because the scale height relevant for ion composition gradients is much smaller than the pressure scale height:  $k_{\rm B}T/m_{\rm p}g \ll P/m_{\rm p}g$ . Therefore the composition gradients driving ordinary diffusion are only significant for sharp concentrations of elements (e.g., pileup at the center) over a much smaller scale than gravitational sedimentation of heavy particles through the bulk of the interior, and thus ordinary diffusion can be neglected for the bulk heating that we are studying here.

According to Equation (17), clusters of  $\langle N \rangle = 100$  particles correspond to a factor of 16 enhancement to the rate of diffusion (and corresponding sedimentation heating). We hypothesize that these Ne clusters will form and enhance diffusion only in strongly liquid conditions past some critical threshold of  $\Gamma_{\rm Ne}^{\rm crit}$ , which is a free parameter in our models. On the other hand, no enhancement to diffusion will occur for WDs that have not yet cooled enough to approach strongly liquid interiors and crystallization. The only two free parameters for this theory are  $\langle N \rangle$  and  $\Gamma_{\rm Ne}^{\rm crit}$ . The enhancement to diffusion given by Equation (17) is active for an interior region from the time it passes the threshold for cluster formation until it crystallizes, transitioning into the solid state and freezing out diffusion.

### 5.1. MESA Models Including Cluster Diffusion

We now show that clusters of size  $\langle N \rangle \gtrsim 1000$  are required for an enhancement to diffusion that is sufficient to provide a cooling delay on the order of several gigayears. Figure 7 shows cooling delays for MESA C/O WD models that implement the enhancement to diffusion according to Equation (17) with  $\langle N \rangle = 300\text{--}3000$  and the onset of clustering at  $\Gamma_{\text{Ne}}^{\text{crit}} = 300$  ( $\Gamma \approx 170$ ). These WD models are descended from metal-rich

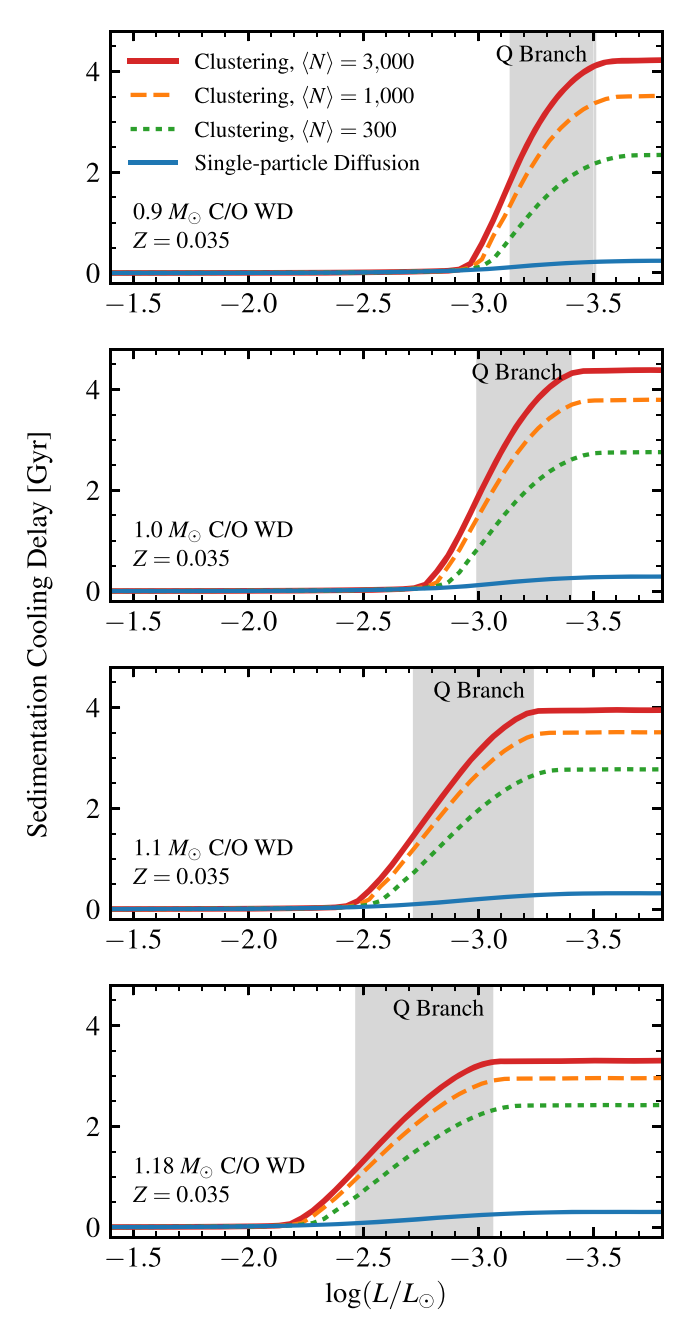
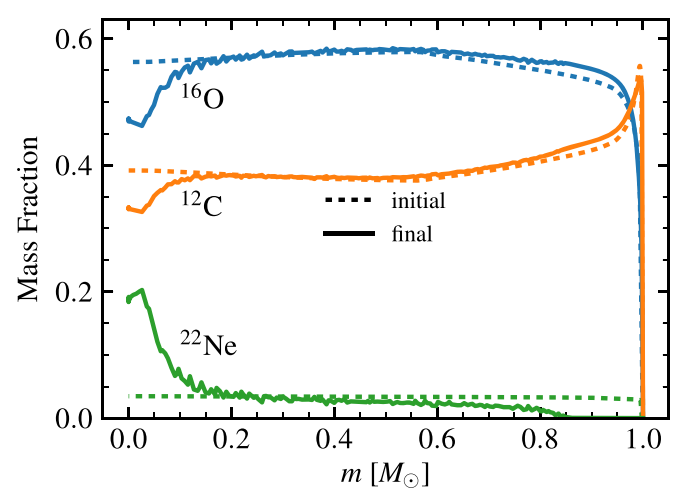
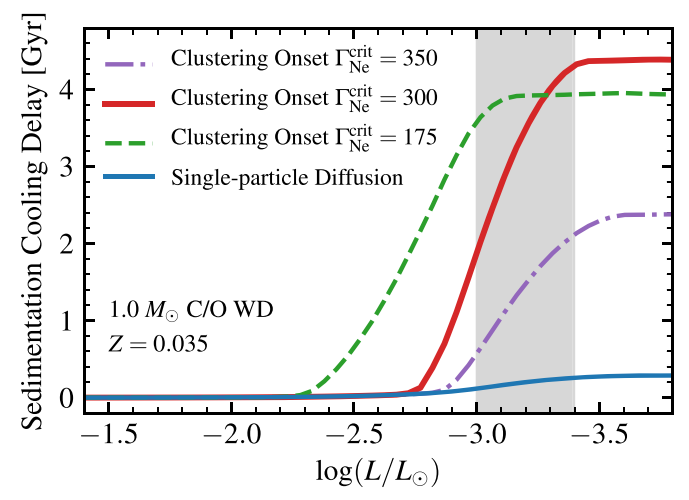


Figure 7. Accumulated cooling delay due to sedimentation heating relative to models that include no sedimentation heating. Blue curves show the cooling delay for models where  $^{22}\mathrm{Ne}$  sediments as single particles as in Figure 5, while the other curves show the delay for models in which sedimentation occurs via  $^{22}\mathrm{Ne}$  clusters according to Equation (17) with  $\Gamma_\mathrm{Ne}^\mathrm{crit}=300$  and various values of  $\langle N \rangle$ . The gray-shaded region labeled "Q branch" shows the luminosity range where interior crystallization occurs, corresponding to the solid contours bracketing the Q branch in Figure 3.

progenitors (Z=0.035), so their interiors are rich in  $^{22}$ Ne, and their cooling delays represent the longest delays that C/O WDs can achieve from sedimentation. Figure 8 shows how the  $^{22}$ Ne profile is rearranged in the interior over the course of cluster sedimentation. Models with  $\langle N \rangle > 3000$  tend to achieve cooling delays similar to the  $\langle N \rangle = 3000$  case, with  $^{22}$ Ne quickly sedimenting inward as soon as local conditions pass the threshold for cluster formation. The overall cooling delay is not particularly sensitive to  $\langle N \rangle$  beyond the value of 3000 needed to speed heating enough to achieve this several gigayear delay. It



**Figure 8.** Interior composition profiles before and after sedimentation for the 1.0  $M_{\odot}$  C/O WD model from Figure 7 with diffusion of  $\langle N \rangle = 3000$  clusters.



**Figure 9.** Comparison of cooling delays for different values of  $\Gamma_{\rm Ne}$  at which clustering begins to occur in a 1.0  $M_{\odot}$  C/O WD.  $\langle N \rangle = 3000$  for each of the models including clustering here.

is possible that once conditions pass the threshold for cluster formation, <sup>22</sup>Ne simply "rains" toward the center in clusters that continually grow as they encounter other Ne particles while sinking.

On the other hand, the delays in these models are quite sensitive to the value of  $\Gamma_{\text{Ne}}^{\text{crit}}$  where the onset of clustering occurs. Figure 9 shows a comparison of cooling delays for a WD model in which only this parameter is varied. For models in which clustering occurs earlier than  $\Gamma_{\text{Ne}}^{\text{crit}}=300$ , the cooling delay mostly accumulates prior to the point where the WD has cooled enough to reach the Q branch, and the overall magnitude of the delay is smaller because the sedimentation heating is released while the WD radiates it away at a higher luminosity. We therefore rule out the onset of significant clustering for  $\Gamma_{\text{Ne}} \lesssim 300$  as inconsistent with the observed CMD location and overall magnitude of the cooling delay inferred by Cheng et al. (2019). For models where  $\Gamma_{\text{Ne}}^{\text{crit}}$  is much larger than 300, the extent of the range where clustering can operate is limited before crystallization halts diffusion at  $\Gamma_{\text{Ne}} \approx 1.8 \times 230 \approx 410$ , so we find that the total delay is maximized around  $\Gamma_{\text{Ne}}^{\text{crit}} = 300$  in our models. We note however that our WD cooling models do not include any fluid

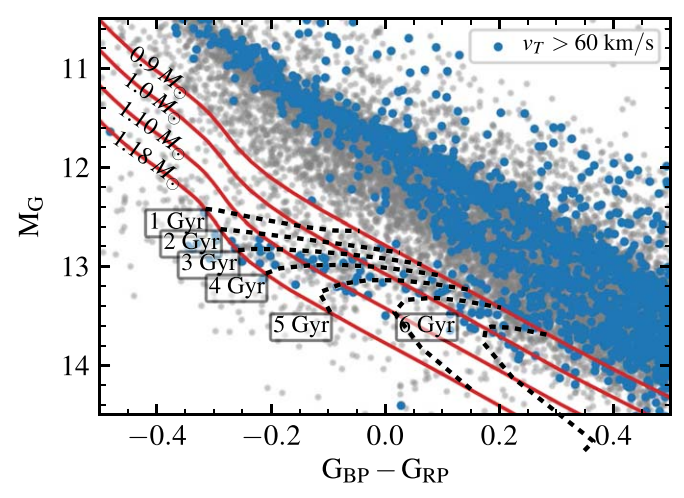


**Figure 10.** C/O WD cooling tracks on the Gaia CMD in the region of the Q branch. Black-dashed curves represent contours of constant WD cooling age (not including prior main sequence lifetime) for WD models including  $^{22}$ Ne sedimentation heating enhanced by clustering for  $\Gamma_{\rm Ne} > 300$ .

instabilities that might be triggered in the interior by the rearranged  $^{22}\mathrm{Ne}$  profile during intermediate stages of sedimentation. When enhanced  $^{22}\mathrm{Ne}$  sedimentation begins near the center, it may leave behind a region depleted of  $^{22}\mathrm{Ne}$  that sits beneath  $^{22}\mathrm{Ne}$ -rich material. The resulting molecular weight gradient could drive dynamical mixing (e.g., Mochkovitch 1983; Brooks et al. 2017) that further enhances the net transport of  $^{22}\mathrm{Ne}$  toward the center. It is currently difficult to account for heating associated with this dynamical mixing in MESA WD models, so we leave exploration of these details for future work. This may lead to even longer delays than our models currently exhibit, particularly for  $\Gamma_{\mathrm{Ne}}^{\mathrm{crit}} > 300$  where it would extend the region of the star where enhanced heating can operate to encompass a much larger portion of the WD core.

Figure 10 shows cooling tracks and contours of constant cooling age on the Gaia CMD for C/O WD models that include sedimentation heating with diffusion enhanced according to Equation (17) with  $\langle N \rangle = 3000$  and the onset of clustering at  $\Gamma_{Ne}^{crit}=300$ . The slowdown in the cooling rate is evident in the higher density of these contours in the region of the Q branch. For the Q branch to host enough fast-moving WDs ( $v_T > 60 \text{ km s}^{-1}$ ), Cheng et al. (2019) calculated that the delayed population should experience an 8 Gyr delay even after accounting for latent heat and merger delays. This value may be reduced to ≈6 Gyr for a younger thick disk age (e.g., Mackereth et al. 2019) or a higher age-velocity-dispersion relation, or if a quickly decreasing star formation history is adopted. Our MESA models exhibit a 4 Gyr delay for metallicity Z = 0.35 progenitors without considering phase separation. Thus, our models provide most of the cooling delay needed to explain velocity observations, though a small tension between these models and observation still exists. Cheng et al. (2019) used O/Ne models for inferences of the cooling delay when  $M \ge 1.1 M_{\odot}$  on the Q branch, so the C/O core compositions for our ultramassive models would imply an additional delay of 1-2 Gyr due to later crystallization and phase separation. DA and DQ WDs may also exhibit small differences from our DB models in sedimentation cooling delays due to minor variations in the L- $T_{core}$  relation. The remaining 2-4 Gyr of cooling delay is likely explained by

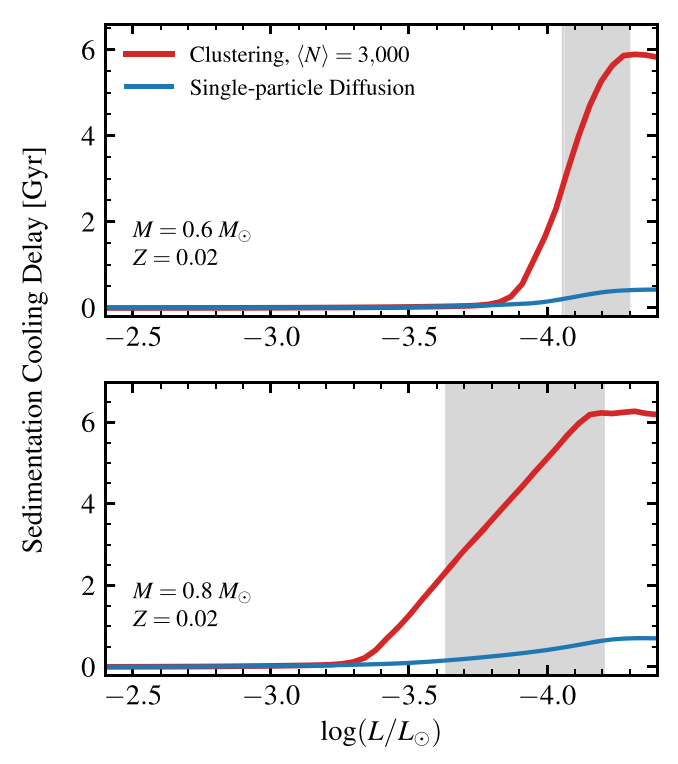


**Figure 11.** Cooling delay due to sedimentation heating relative to models that include no sedimentation heating. Gray-shaded regions indicate the luminosity range over which crystallization is occurring in the interior.

some combination of these smaller effects or other dynamical mixing that we have not considered in our models here.

### 5.2. Predictions for Lower-mass WDs

With the free parameters of our clustering model tuned to match the observations of ultramassive WDs on the Q branch, this model makes predictions for the cooling rates of less massive WDs. The WD models in this section are constructed using the MESA test case make\_co\_wd in version r10398. We vary initial mass and metallicity to produce WDs of the desired mass, and save the WD model when it cools to a luminosity of  $10~L_{\odot}$ . For initial Z=0.02, an initial mass of  $3.25~M_{\odot}$  produces a  $0.6~M_{\odot}$  WD, and  $4.25~M_{\odot}$  produces a  $0.8~M_{\odot}$  WD. For initial Z=0.04, these initial masses are  $3.1~M_{\odot}$  and  $4.2~M_{\odot}$ . The AGB winds in these models leave some hydrogen in the atmosphere, so when diffusion is turned on, the models quickly become DA WDs. Our WD cooling calculations for these models use MESA r12115 as in previous sections.

Figure 11 shows the cooling delays for  $0.6~M_{\odot}$  and  $0.8~M_{\odot}$  WDs descended from progenitor stars with metallicity Z=0.02. Even though this lower metallicity leaves less <sup>22</sup>Ne in the WD interior compared to the models in the previous section, sedimentation of <sup>22</sup>Ne powers a longer cooling delay ( $\approx 6~\rm Gyr$ ) in these lower-mass models because crystallization occurs at a much lower luminosity.

Clustering may provide a natural explanation for the recent observations of Kilic et al. (2020), who noted that the M- $T_{\rm eff}$  distribution of DA WDs warmer than 6000 K shows an excess of WDs in the mass range 0.7–0.9  $M_{\odot}$ . The location of this pileup is coincident with the expected location of crystallization. However, by comparing the data with cooling models that include latent heat release during crystallization, Kilic et al.

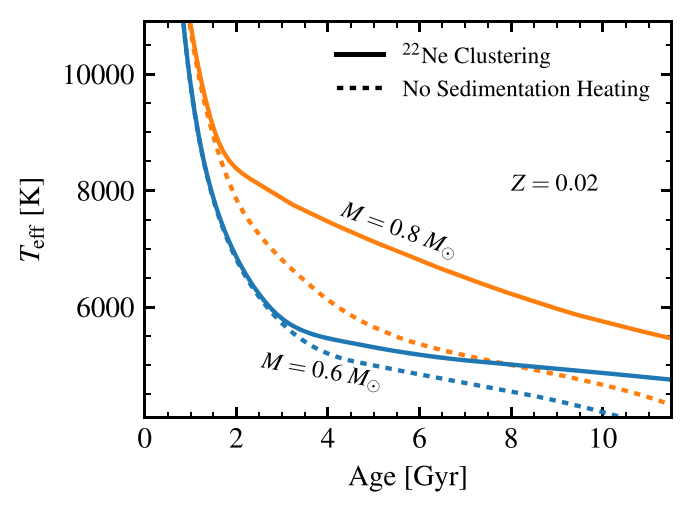


**Figure 12.** Effective temperature evolution for 0.6 and 0.8  $M_{\odot}$  models with and without sedimentation heating from <sup>22</sup>Ne clusters.

(2020) showed that the latent heat alone does not lead to cooling delays sufficient to explain the observed distribution.

Figures 11 and 12 show that a 0.8  $M_{\odot}$  model will experience a significant extra delay due to  $^{22}$ Ne clustering coincident with crystallization and consistent with the temperatures of the excess WDs observed by Kilic et al. (2020). On the other hand, clustering will have no effect on the cooling inferences for 0.6  $M_{\odot}$  WDs near the peak of the WD mass distribution in the Kilic et al. (2020) sample because it is limited to  $T_{\rm eff} > 6000$  K. Clustering and crystallization do not begin for 0.6  $M_{\odot}$  WDs until they cool below  $T_{\rm eff} < 6000$  K.

Due to its high metallicity,  $Z \approx 0.04$ , the open cluster NGC 6791 was noted by Deloye & Bildsten (2002) as an important environment to probe the impact of  $^{22}$ Ne sedimentation on WD cooling. This proved to be the case when the measured WD luminosity function (WDLF) revealed a peak at  $\log(L/L_{\odot}) \approx -4.0$  that yielded the faintest WDs in the cluster (Bedin et al. 2008). These WDs should have an age matching the cluster age of  $8.2 \pm 0.3$  Gyr (McKeever et al. 2019). However, standard WD cooling models that do not include  $^{22}$ Ne sedimentation indicate an age of only 6 Gyr (Bedin et al. 2008). García-Berro et al. (2010) and Althaus et al. (2010c) showed that including C/O phase separation along with (single-particle)  $^{22}$ Ne sedimentation provides a WD cooling delay that is long enough to alleviate this discrepancy.

Figure 13 shows WD cooling models for 0.57 and 0.6  $M_{\odot}$ WDs with Z = 0.04, representing the WD mass range likely to dominate the WDLF peak in NGC 6791. As previously noted by Bedin et al. (2008), models that do not include sedimentation become too faint after 6 Gyr. Our models that include <sup>22</sup>Ne clustering experience significant cooling delays, but still reach the faint peak of the WDLF in the cluster age of 8 Gyr. In García-Berro et al. (2010), the addition of phase separation and single-particle <sup>22</sup>Ne sedimentation shifted the brightness of the faint peak in the theoretical WDLF at 8 Gyr by  $\approx$  -0.5 mag to bring models into agreement with the observed WDLF. Comparing the two sets of curves in Figure 13 at 8 Gyr, our models that include  $^{22}$ Ne clustering have  $\approx +0.2$  dex higher luminosity than those with no sedimentation heating. This would shift a theoretical WDLF by  $\approx$  -0.5 mag. Although our models do not include C/O phase separation during crystallization, including an additional delay of  $\approx 1$  Gyr due to phase separation would not significantly change the WDLF at the

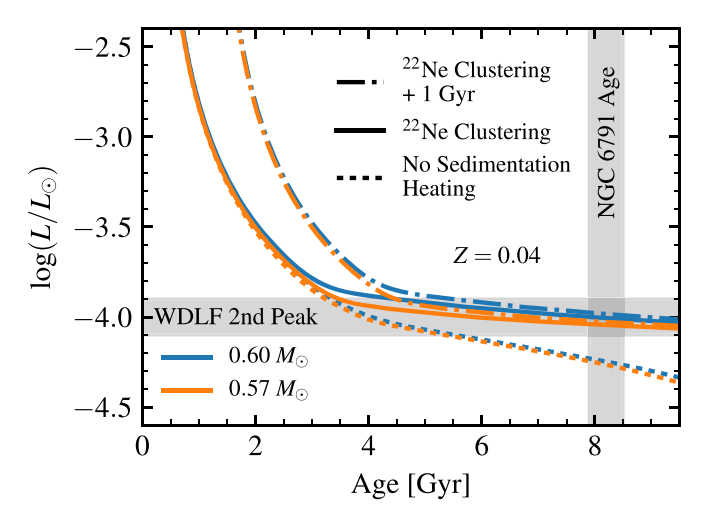


**Figure 13.** Luminosity evolution of 0.57 and  $0.6 M_{\odot}$  WDs compared to constraints from observations of the open cluster NGC 6791. Gray-shaded regions show the cluster age (McKeever et al. 2019) and faint edge of the WD luminosity function (Bedin et al. 2008).

cluster age of 8 Gyr where the evolution is already very slow. We show this in Figure 13 by including dotted–dashed curves with an artificial extra delay of 1 Gyr in addition to the  $^{22}\mathrm{Ne}$  clustering. At the cluster age of 8 Gyr, the luminosities for these curves are just 5% higher, or  $\approx\!0.05$  mag brighter. Thus, the total shift in the WDLF including both  $^{22}\mathrm{Ne}$  clustering and C/O phase separation might be as large as  $\approx\!-0.55$  mag, which would still agree with the  $\approx\!-0.5$  mag shift calculated by García-Berro et al. (2010) to well within the photometric uncertainties ( $\approx\!0.15$  mag). Therefore, the addition of  $^{22}\mathrm{Ne}$  clustering does not bring theoretical cooling models into tension with the observations of NGC 6791.

### 6. Conclusions

We summarize our main arguments as follows:

- 1. A subset (5%-10%) of massive and ultramassive WDs  $(0.9-1.3\,M_{\odot})$  experience a cooling delay of several gigayears that is too long to be explained by crystallization, phase separation, chemical differentiation due to diffusion, or any plausible combination of these effects.
- 2. The evolutionary phase where the cooling delay occurs coincides with the regime for a C/O phase transition from liquid to solid in the WD core.
- 3. Heating due to sedimentation of <sup>22</sup>Ne in C/O WD cores can provide enough luminosity for a several gigayear cooling delay prior to crystallization, but only if sedimentation can proceed much faster than predicted by the diffusion coefficients of individual <sup>22</sup>Ne ions, which are theoretically well constrained.
- 4. We therefore propose that in the strongly liquid regime,  $^{22}$ Ne ions can form into solid clusters of  $\langle N \rangle \gtrsim 1000$  particles that are heavier and sediment toward the center faster according to Stokes–Einstein drift, and our MESA models show that this modification creates a  $\approx$ 4 Gyr cooling delay, explaining most of the cooling delay for fast-moving WDs on the Q branch.

Our simple model for clustering leaves the size of clusters  $(\langle N \rangle)$  as a free parameter, as well as the value of Coulomb coupling for Ne at which clusters begin to form  $(\Gamma_{Ne}^{crit})$ . While we have not explored a first-principles physical approach for

constraining how these clusters form, it may be that MD modeling of strongly coupled plasmas (e.g., Daligault 2006a; Horowitz et al. 2010; Hughto et al. 2010) can provide more insight into the physics of this cluster formation. It may also be the case that solid clusters form with some other composition than pure Ne. In that case, it would still be straightforward to reinterpret our sedimentation numbers for solid clusters composed of a Ne-rich C/O/Ne mixture that sinks relative to the liquid C/O background.

The subset of ultramassive WDs that experience this extra cooling delay of several gigayears due to <sup>22</sup>Ne sedimentation likely descends from an old, metal-rich population. In particular, the <sup>22</sup>Ne in WD cores forms from the primordial CNO abundance of their progenitor stars, so these WDs are likely associated with the high  $[\alpha/Fe]$  sequence of old stars in the galactic disk population (Nidever et al. 2014; Hayden et al. 2015; Mackereth et al. 2019; Sharma et al. 2020). Early in galactic history, core-collapse supernovae produced the CNO necessary to seed the eventual production of <sup>22</sup>Ne in these old WD cores. The WDs that experience the longest delays in our model would be those descended from the highest  $\alpha$ -abundance progenitors, and the distribution of cooling delays for this sample of WDs should be correlated with the  $\alpha$ -abundance distribution of other old stars within a few hundred parsecs of the Sun (Castro et al. 1997; Pompéia et al. 2003; Khoperskov et al. 2020). Our ultramassive C/O WD models may represent C/O WD merger products, so the final <sup>22</sup>Ne abundance may also be modestly enhanced by burning during the merger process (see Section 2). As most WDs would have lower <sup>22</sup>Ne abundances, they would experience much less sedimentation heating, which naturally explains why Cheng et al. (2019) inferred that only a small fraction of WDs experience a substantial extra cooling delay. We therefore conclude that the sedimentation of clustered <sup>22</sup>Ne can explain most of the cooling delay on the Q branch, though some tension between theoretical prediction and observations may still exist (Section 5.1).

Our model also predicts that lower-mass (0.6– $0.9\,M_{\odot})$  WDs experience a substantial cooling delay ( $\gtrsim$ 6 Gyr for  $Z \geqslant 0.02$ ) very late in their evolution. This likely explains the excess of 0.7– $0.9\,M_{\odot}$  WDs recently observed by Kilic et al. (2020). This cooling delay would also have a large impact on the faint edge of the WD luminosity function in old, metal-rich star clusters. While high metallicity is rare for old globular clusters (e.g., Hansen et al. 2002; Hansen et al. 2007; Campos et al. 2016), we have shown that for the old, metal-rich open cluster NGC 6791, our model produces WD cooling consistent with the main sequence turnoff age and WD luminosity function.

Although we have shown that WDs with O/Ne cores are unlikely to account for the cooling anomaly on the Q branch, our clustering model does predict that O/Ne WDs should also experience a significant cooling delay coincident with interior crystallization. The  $^{23}$ Na present in all O/Ne WD cores should also be susceptible to the clustering process that we have described for  $^{22}$ Ne. The charge contrast between  $^{23}$ Na ( $Z_i = 11$ ) and the O/Ne background is somewhat smaller than that of  $^{22}$ Ne to C/O, so clustering would begin later and possibly only lead to a delay of a few gigayears, but this would still slow the cooling rate of O/Ne WDs by a factor of a few. This only makes it more striking that Figure 2 shows no feature corresponding to O/Ne WD crystallization on the CMD, and

may imply a stricter constraint on the fraction of O/Ne WDs among ultramassive WDs.

When neither  $^{22}$ Ne and  $^{23}$ Na are present in a WD interior, clustering of other elements may play an important role in WD cooling. For  $^{56}$ Fe present at mass fraction  $X_{\rm Fe} \sim 0.001$ , Equation (5) predicts possible gigayear delays if clustering can enhance sedimentation sufficiently. Even in He WD cores that never crystallize, the large charge contrast of heavier trace elements may put them in the clustering regime (Equation (14)), and the chemical potential for clusters of elements such as  $^{14}$ N could drive significant stratification and heating even without the weight of extra neutrons (Appendix C).

We are grateful to the anonymous referee for many suggestions that improved this paper. We thank Odette Toloza, Boris Gänsicke, and Detlev Koester for providing tabulated atmospheric boundary conditions for DB WDs. We are grateful to Bart Dunlap and J.J. Hermes for valuable discussions about DQ WDs and WD mergers, and to Mike Rich for discussion of galactic metallicity distributions. We are grateful to Andrew Cumming and Chuck Horowitz for sharing insights on crystallization in multicomponent plasmas.

This work was supported by the National Science Foundation through grants PHY-1748958 and ACI-1663688. This research benefited from interactions that were funded by the Gordon and Betty Moore Foundation through grant GBMF5076. This work used the Extreme Science and Engineering Discovery Environment (XSEDE; Towns et al. 2014), which is supported by National Science Foundation grant No. ACI-1548562, specifically *comet* at the SDSC through allocation TG-AST180050. Support for this work was provided by NASA through Hubble Fellowship grant # HST-HF2-51382.001-A awarded by the Space Telescope Science Institute, which is operated by the Association of Universities for Research in Astronomy, Inc., for NASA, under contract NAS5-26555. J.S. is also supported by the A.F. Morrison Fellowship in Lick Observatory.

Software: MESA (Paxton et al. 2011, 2013, 2015, 2018, 2019), ipython/jupyter (Pérez & Granger 2007; Kluyver et al. 2016), matplotlib (Hunter 2007), NumPy (van der Walt et al. 2011), and Python from https://www.python.org.

# Appendix A Derivation of Fundamental Equations

A star is a system with properties that are functions of both space and time. Equilibrium thermodynamic systems have homogeneous properties (i.e., the system has *a* temperature) that do not vary with time. Time evolution is typically introduced by thinking about moving through a sequence of equilibrium states. The consideration of spatial variation proceeds by dividing the star into infinitesimal systems (but not so infinitesimal that thermodynamics breaks down) and taking the continuum limit. These infinitesimal subsystems are *open* systems that exchange both heat and matter with their surroundings.

# A.1. The "First Law" and Conservation of Energy

The "first law" is a statement that encodes energy conservation. Chapter II of de Groot & Mazur (1969)

demonstrates how to formulate the first law in a multispecies system where each species is allowed to have a flow relative to the mean. We follow their discussion, but specialize to our problem when it allows simplification. In order to allow easy comparison with Paxton et al. (2018), we use the indices s and t to refer to particle species.

The hydrodynamic equations come directly from moments of the collisional Boltzmann equation (see, e.g., Chapter 7 of Hirschfelder et al. 1964). When considering the evolution of quantities that are conserved in collisions (mass, momentum, and energy), sums of the collision integrals over all species vanish, yielding simpler equations for their rate of change.

We assume a fully ionized plasma of S species (electrons plus S-1 species of ions). With no reactions, continuity of each species yields

$$\frac{\partial \rho_s}{\partial t} + \boldsymbol{\nabla} \cdot (\rho_s \boldsymbol{\nu}_s) = 0. \tag{A1}$$

The total mass density is

$$\rho = \sum_{s} \rho_{s},\tag{A2}$$

and we define the velocity v as the barycentric velocity,

$$\mathbf{v} \equiv \frac{1}{\rho} \sum_{s} \rho_{s} \mathbf{v}_{s}. \tag{A3}$$

We define relative velocities for each species as  $w_s = v_s - v$ . Summing the individual continuity equations (Equation (A1)) and using the definitions above gives mass conservation

$$\frac{\partial \rho}{\partial t} + \boldsymbol{\nabla} \cdot (\rho \boldsymbol{v}) = 0. \tag{A4}$$

The inviscid momentum equation is

$$\frac{\partial(\rho \mathbf{v})}{\partial t} + \nabla \cdot (\rho \mathbf{v} \otimes \mathbf{v}) = -\nabla P + \sum_{s} f_{s}, \tag{A5}$$

where P is the (scalar) pressure and  $\otimes$  represents the outer product. We assume that the relative velocities,  $w_s$ , are much less than the thermal velocities, such that the full pressure tensor is dominated by its scalar component (the equilibrium pressure). The force density on species s is

$$f_s = n_s F_s = n_s (m_s \mathbf{g} + q_s E), \tag{A6}$$

where  $n_s$  is the number density,  $m_s$  is the mass, g is the gravitational acceleration,  $q_s$  is the charge, and E is the electric field. Local charge neutrality  $(\sum_s n_s q_s = 0)$  implies that the total force is simply the gravitational force,

$$\sum_{s} \mathbf{f}_{s} = \rho \mathbf{g}. \tag{A7}$$

When in hydrostatic equilibrium, if the ion contribution to the total pressure is negligible (meaning  $P \approx P_{\rm e}$ ), the electron equilibrium requires an approximate balance between the pressure gradient and the electric force. This implies the presence of an electric field

$$E \approx -\frac{\rho \mathbf{g}}{\sum_{\text{ions}} n_s q_s}.$$
 (A8)

The equation for the specific (per unit mass) internal energy, u, is

$$\frac{\partial(\rho u)}{\partial t} + \boldsymbol{\nabla} \cdot (\rho u \boldsymbol{v}) = -\boldsymbol{\nabla} \cdot \boldsymbol{J}_q + \rho \dot{q} - P \boldsymbol{\nabla} \cdot \boldsymbol{v} 
+ \sum_{s} \boldsymbol{w}_s \cdot \boldsymbol{f}_s, \tag{A9}$$

where  $\dot{q}$  reflects the rate of processes that can directly remove energy from the system (i.e., optically thin cooling) and where  $J_q$  is the "heat flow" vector (e.g., thermal conduction or radiative transfer). Denoting the Lagrangian time derivative as D/Dt, the flow of energy into a Lagrangian parcel is

$$\frac{Dq}{Dt} = \dot{q} - \frac{1}{\rho} \boldsymbol{\nabla} \cdot \boldsymbol{J}_q, \tag{A10}$$

which when combined with the Lagrangian derivative of specific internal energy,

$$\frac{Du}{Dt} = \frac{1}{\rho} \left[ \frac{\partial(\rho u)}{\partial t} + \boldsymbol{\nabla} \cdot (\rho u \boldsymbol{v}) \right],\tag{A11}$$

yields

$$\frac{Du}{Dt} = \frac{Dq}{Dt} - P\frac{D}{Dt} \left(\frac{1}{\rho}\right) + \frac{1}{\rho} \sum_{s} \mathbf{w}_{s} \cdot \mathbf{f}_{s}. \tag{A12}$$

When  $w_s = 0$ , Equation (A12) reduces to the familiar thermodynamic relation

$$\frac{Dq}{Dt} = \frac{Du}{Dt} + P \frac{D}{Dt} \left(\frac{1}{\rho}\right),\tag{A13}$$

which is also Equation (60) in Paxton et al. (2018).

The  $w_s$  do not lead to a net transport of mass  $(\sum_s \rho_s w_s = 0)$  or of charge  $(\sum_s q_s n_s w_s = 0)$ . With the force density of Equation (A6), these constraints mean that the final term of Equation (A12) vanishes even for nonzero  $w_s$ . Therefore, the first law expression in Paxton et al. (2018) need not be modified, even in this nonequilibrium circumstance.

### A.2. Entropy and the Second Law

The entropy is a quantity that can be defined in terms of the macroscopic characteristics of the system. We make the assumption that, even though the star itself is not in equilibrium, there are small mass elements in a local equilibrium where the local entropy is well characterized. It is often useful to characterize heating by a physical process like mixing in terms of entropy generation and evolution (e.g., Beznogov & Yakovlev 2013), so here we derive the relationship between entropy and the thermodynamic relations of the previous section. If we write the internal energy, U, of such an element in terms of the independent thermodynamic basis variables  $(S, V, N_s)$ , then expanding yields the thermodynamic identity

$$dU = TdS - PdV + \sum_{s} \mu_{s} dN_{s}, \tag{A14}$$

where S is the entropy and T is the temperature. The sum runs over all species present and  $\mu_s$  is the chemical potential for species s. Writing these differentials as time derivatives and

casting in specific (per unit mass) form gives

$$T\frac{Ds}{Dt} = \frac{Du}{Dt} + P\frac{D}{Dt} \left(\frac{1}{\rho}\right) - \sum_{s} \mu_{s} \frac{D}{Dt} \left(\frac{n_{s}}{\rho}\right). \tag{A15}$$

From continuity (both individual species and total),

$$\frac{D}{Dt} \left( \frac{n_s}{\rho} \right) = -\frac{1}{\rho} \boldsymbol{\nabla} \cdot (n_s \boldsymbol{w}_s), \tag{A16}$$

so that

$$T\frac{Ds}{Dt} = \frac{Du}{Dt} + P\frac{D}{Dt} \left(\frac{1}{\rho}\right) + \frac{1}{\rho} \sum_{s} \mu_{s} \boldsymbol{\nabla} \cdot (n_{s} \boldsymbol{w}_{s}). \tag{A17}$$

Combining with Equation (A12) and manipulating the term with the divergence, we have

$$T\frac{Ds}{Dt} = \frac{Dq}{Dt} + \frac{1}{\rho} \sum_{s} \mathbf{w}_{s} \cdot \mathbf{f}_{s} + \frac{1}{\rho} \sum_{s} [\nabla \cdot (n_{s} \mu_{s} \mathbf{w}_{s}) - n_{s} \mathbf{w}_{s} \cdot \nabla \mu_{s}].$$
(A18)

We can rearrange terms to write

$$T\frac{Ds}{Dt} = \frac{Dq}{Dt} + \frac{1}{\rho} \sum_{s} \nabla \cdot (n_{s} \mu_{s} w_{s}) + \frac{1}{\rho} \sum_{s} w_{s} \cdot (f_{s} - n_{s} \nabla \mu_{s}).$$
(A19)

Note that in the notation of Beznogov & Yakovlev (2013) this last term in parentheses is  $n_s \tilde{F}_s$ . They say this term (their Equation (20)) is the rate of specific entropy generation via collisions. We will see that is true in the case of constant T (which they assume early on).

Note that this collisional entropy production in the final term of Equation (A19) need not always be associated with production of "heat," as there is freedom in Equation (A19) for a suitably defined entropy of mixing with Dq/Dt = 0. In terms of implementation, this implies that the basis for defining the specific entropy s in an EOS must be consistent with the composition degrees of freedom where mixing may produce entropy if Equation (A19) is to be used. For example, an EOS that defines the compositional dependence of entropy in terms of only the average particle mass would not be adequate for using Equation (A19) to study entropy generation by sedimentation of multiple distinct species of particles with the same mass.

By defining the entropy flow as

$$\mathbf{J}_{s} = \frac{1}{T} \left( \mathbf{J}_{q} - \sum_{s} \mu_{s} n_{s} \mathbf{w}_{s} \right), \tag{A20}$$

we can rewrite Equation (A19) as an entropy balance equation

$$\rho \frac{Ds}{Dt} = -\boldsymbol{\nabla} \cdot \boldsymbol{J_s} + \sigma, \tag{A21}$$

where the entropy generation rate is

$$\sigma = \frac{\rho}{T} \frac{Dq}{Dt} - \frac{1}{T^2} \mathcal{J}_q \cdot \nabla T + \frac{1}{T} \sum_{s} \mathbf{w}_s \cdot \left( \mathbf{f}_s - n_s T \nabla \frac{\mu_s}{T} \right). \tag{A22}$$

Setting Dq/Dt=0, so that one can meaningfully define a closed system, then the constraint that each term in  $\sigma$  must be non-negative leads to the satisfaction of the second law of thermodynamics. In Chapter III, de Groot & Mazur (1969) discuss these points further and show several equivalent ways of writing this expression using different definitions of the heat flow.

# Appendix B Implementation of Sedimentation Heating

We now revisit the energetics of gravitational settling and demonstrate the relationship between the Paxton et al. (2018) and García-Berro et al. (2008) approaches. This clarifies the approximation being made in MESA.

### B.1. Description of Approaches

When formulating the stellar structure equations, energy conservation is included by considering the energy flow in and out of a fluid parcel (e.g., Kippenhahn et al. 2012, Chapter 4). In this Lagrangian picture, to understand how the energy of a fluid parcel is changing, we account for the specific (per unit mass) rate of energy injection into the parcel,  $\epsilon$ , and the specific rate of energy flow through the boundaries,  $\partial L/\partial m$ . The specific heating rate (Dq/Dt) for the parcel then satisfies

$$\frac{Dq}{Dt} = \epsilon - \frac{\partial L}{\partial m}.$$
 (B1)

Using Equation (A13), this is traditionally rewritten in terms of a source function  $\epsilon_{grav}$ , such that

$$\frac{\partial L}{\partial m} = \epsilon + \epsilon_{\text{grav}},$$
 (B2)

with

$$\epsilon_{\text{grav}} \equiv -\frac{Du}{Dt} - P\frac{D}{Dt} \left(\frac{1}{\rho}\right).$$
 (B3)

### B.1.1. Approach in García-Berro et al. (2008)

García-Berro et al. (2008) followed this approach, with  $\epsilon = -\epsilon_{\nu}$  (only optically thin neutrino cooling, no nuclear reactions). They restricted themselves to a composition with two chemical elements, so that  $X_{22} + X_b = 1$ . When Du/Dt was evaluated in the  $(\rho, T, X_{22})$  basis, they derived their Equation (5), which in our notation is

$$\frac{\partial L}{\partial m} = -\epsilon_{\nu} + \frac{T}{\rho^{2}} \left( \frac{\partial P}{\partial T} \right)_{\rho,X} \frac{D\rho}{Dt} - c_{V} \frac{DT}{Dt} - \left( \frac{\partial u}{\partial X_{22}} \right)_{\rho,T} \frac{DX_{22}}{Dt},$$
(B4)

where  $c_V = (\partial u/\partial T)_{\rho,X}$  is the specific heat at constant volume. We identify the effective García-Berro et al. (2008) <sup>22</sup>Ne

García-Berro et al. (2008) label their species with subscripts 1 and 2. We label their species "1" with "22" to indicate it is  $^{22}$ Ne; we label quantities associated with their species "2" with "b" (to represent the background).

heating term as

$$\epsilon_{22} \equiv -\left(\frac{\partial u}{\partial X_{22}}\right)_{o,T} \frac{DX_{22}}{Dt}.$$
 (B5)

### B.1.2. Approach in Paxton et al. (2018)

When evaluating the total derivative of the internal energy in Equation (B3), a common approximation is to neglect the composition derivatives. This is the default approach adopted in MESA, justified by the fact that these terms are negligible compared to the energy released by nuclear reactions (e.g., Kippenhahn et al. 1965). When  $(\rho, T, \{X_i\})$  are the structure variables, the usual form of  $\epsilon_{\text{grav}}$  in MESA is given in Equation (12) of Paxton et al. (2011) or Equation (65) of Paxton et al. (2018):

$$-\epsilon_{\text{grav}} = c_P T \left[ (1 - \nabla_{\text{ad}} \chi_T) \frac{D \ln T}{Dt} - \nabla_{\text{ad}} \chi_\rho \frac{D \ln \rho}{Dt} \right]. \quad (B6)$$

The thermodynamic derivatives have their usual definitions:  $c_P = (\partial e/\partial T)_{P,X},$   $\chi_T = (\partial \ln P/\partial \ln T)_{\rho,X},$   $\chi_\rho = (\partial \ln P/\partial \ln \rho)_{T,X},$  and  $\nabla_{\rm ad} = (\partial \ln T/\partial \ln P)_{s,X}.$  Equation (B6) is identical (after using thermodynamic and mathematical identities) to the non- $\epsilon_{22}$  terms in Equation (B4).

Evaluating the neglected composition derivative terms can be difficult in a code like MESA when accounting for a mixture of more than a few elements. The model evolves the set of mass fractions specified by the choice of nuclear network. However, this structural basis  $(\rho, T, \{X_i\})$  usually does not match the basis of the EOS. For the  $(\rho, T)$ -basis EOSes relevant for WDs in MESA, the composition basis for HELM is  $(\langle A \rangle, \langle Z_i \rangle)$ , while the composition basis for PC is all isotopes with mass fractions above some threshold (default:  $10^{-3}$ ). This makes it challenging (or impossible) to evaluate all the relevant partial derivatives with respect to composition within MESA.

Therefore, instead of attempting to fully evaluate  $\epsilon_{\rm grav}$ , the energetic effects of <sup>22</sup>Ne sedimentation are incorporated into MESA via the inclusion of an additional heating term specific to this isotope. This follows the approach taken by Bildsten & Hall (2001) and Deloye & Bildsten (2002) who evaluated the net power generated by <sup>22</sup>Ne sedimentation in the trace limit. The specific rate at which energy is deposited is then

$$\epsilon_{22} = \frac{|F|v_{22}}{(Am_{\rm p})/X_{22}} = (22m_{\rm p}g - 10eE)\frac{X_{22}v_{22}}{22m_{\rm p}}.$$
 (B7)

The  $^{22}$ Ne diffusion velocity ( $w_{22}$ ) and electric field (E) are calculated in the diffusion routine and then used to evaluate the above heating term. This expression assumes the only isotope settling is  $^{22}$ Ne and assumes it is a trace ( $X_{22} \ll 1$ ). By assuming only two isotopes, García-Berro et al. (2008) also makes the assumption that only  $^{22}$ Ne sediments, though their expression does not explicitly make the trace assumption.  $^9$ 

# B.2. Unification of the Two Approaches

The heating terms in Equations (B5) and (B7) appear different. In particular, the MESA approach indicates that

heating occurs anywhere that the <sup>22</sup>Ne has a finite abundance and a nonzero diffusion velocity, while the García-Berro et al. (2008) approach only indicates heating where the local <sup>22</sup>Ne abundance is changing. WD cooling calculations with MESA were compared with the results from García-Berro et al. (2008) and found to agree (see Section 3.5, Figure 18 in Paxton et al. 2018). But if one inspects the *local* profiles of the <sup>22</sup>Ne heating in MESA and in Figure 4 of García-Berro et al. (2008), the two approaches appear different.

### B.2.1. Approach of García-Berro et al. (2008)

Let us evaluate the total heating rate of sedimentation over the whole star,

$$\dot{E}_{22} = \int \epsilon_{22} dm = -\int dm \left(\frac{\partial u}{\partial X_{22}}\right)_{\rho,T} \frac{DX_{22}}{Dt}.$$
 (B8)

Since there are no nuclear reactions, composition changes are entirely due to gravitational settling, so that

$$\frac{DX_{22}}{Dt} = -\frac{1}{\rho} \nabla \cdot (\rho X_{22} w_{22}).$$
 (B9)

As García-Berro et al. (2008) indicated, in a cool WD the electronic contributions to the internal energy dominate. In the fully degenerate limit,

$$\left(\frac{\partial u}{\partial X_{22}}\right)_{\rho,T} = \left(\frac{\partial u}{\partial Y_{e}}\right)_{\rho,T} \left(\frac{\partial Y_{e}}{\partial X_{22}}\right)$$

$$\approx \frac{\mu_{e}}{m_{p}} \left(\frac{10}{22} - \frac{Z_{b}}{A_{b}}\right) = -\frac{\mu_{e}}{22m_{p}}, \tag{B10}$$

where  $m_{\rm p}$  is the atomic mass unit,  $\mu_{\rm e}$  is the electron chemical potential, and we have assumed the background species has  $Z_b/A_b=1/2$ . Therefore, we have

$$\begin{split} \dot{E}_{22} &= -\frac{1}{22m_{\rm p}} \int \frac{\mu_{\rm e}}{\rho} \boldsymbol{\nabla} \cdot (\rho X_{22} \boldsymbol{w}_{22}) dm \\ &= -\frac{1}{22m_{\rm p}} \int \frac{1}{\rho} [\boldsymbol{\nabla} \cdot (\mu_{\rm e} \rho X_{22} \boldsymbol{w}_{22}) - \rho X_{22} \boldsymbol{w}_{22} \cdot \boldsymbol{\nabla} \mu_{\rm e}] dm \\ &= -\frac{1}{22m_{\rm p}} \left[ \int \frac{\partial}{\partial m} (4\pi r^2 \mu_{\rm e} \rho X_{22} \boldsymbol{w}_{22}) dm \\ &- \int X_{22} \boldsymbol{w}_{22} \cdot \boldsymbol{\nabla} \mu_{\rm e} dm \right] \\ &= \frac{1}{22m_{\rm p}} \int X_{22} \boldsymbol{w}_{22} \cdot \boldsymbol{\nabla} \mu_{\rm e} dm. \end{split} \tag{B11}$$

The manipulation of the divergence is analogous to that in Equation (A18). The first integral on the third line vanishes since the term in parentheses vanishes at the center and the surface. Diffusion changes the local entropy both by transporting entropy and locally generating entropy. Here we see that a term similar to local entropy generation is closely related to the total integrated change in internal energy, while the integrated transport term has no net effect.

The thermal conduction timescale across the WD core is much less than the evolutionary timescale. This has the consequence that the transport term can be neglected. To get the overall cooling right, it does not matter exactly how the heating is deposited, so long as the correct total amount of

 $<sup>\</sup>overline{^9}$  Since  $^{22}$ Ne mass fractions are typically of order the initial metallicity, the trace limit is initially a good approximation. It does become worse as  $^{22}$ Ne centrally concentrates (see, e.g., Figure 8 where the mass fraction reaches  $\approx$ 0.2).

energy is deposited. Thus, an equivalent expression for  $\epsilon_{22}$  is given by the part of the integrand that does not vanish,

$$\epsilon_{22} = \frac{1}{22m_{\rm p}} X_{22} \boldsymbol{w}_{22} \cdot \boldsymbol{\nabla} \mu_{\rm e}. \tag{B12}$$

B.2.2. Approach in Paxton et al. (2018)

Give the final term in Equation (A19) the name

$$\epsilon_{\text{diff}} = \frac{1}{\rho} \sum_{s} \mathbf{w}_{s} \cdot (\mathbf{f}_{s} - n_{s} \nabla \mu_{s}). \tag{B13}$$

As shown in Equation (A22), under the assumption of constant T, this is proportional to the local entropy generation rate due to diffusion. Using the definition of  $f_s$  we write

$$\epsilon_{\text{diff}} = \frac{1}{\rho} \sum_{s} n_s \boldsymbol{w}_s \cdot (m_s \boldsymbol{g} + q_s \boldsymbol{E} - \boldsymbol{\nabla} \mu_s). \tag{B14}$$

To satisfy charge neutrality, the electron flux must be similar to the largest ion fluxes  $|n_e w_e| \sim |n_i w_i|$ . In the strongly degenerate limit, the electrons are responsible for maintaining hydrostatic equilibrium, so that the term in parentheses in Equation (B14) must be very close to zero for electrons. Hence, the sum in Equation (B14) can be restricted to run only over the ion species, since the entropy generation for the electrons is negligible near equilibrium, while the deviations from equilibrium can be much larger for an ion such as  $^{22}$ Ne where  $\nabla \mu_i$  is negligible and the electric and gravitational forces do not cancel.

The electric field estimate of Equation (A8) is

$$E = -\frac{\langle A \rangle m_{\rm p}}{\langle Z_{\rm i} \rangle e} g, \tag{B15}$$

where  $\langle A \rangle$  and  $\langle Z_i \rangle$  are the mean ion mass number and charge number, respectively. Dropping the ion chemical potentials and using this estimate of the electric field in Equation (B14) gives

$$\epsilon_{\text{diff}} = \frac{1}{\rho} \sum_{\text{ions}} \mathbf{w}_s \cdot \mathbf{g} \left( \rho_s - n_s Z_s \frac{\langle A \rangle m_p}{\langle Z_i \rangle} \right). \tag{B16}$$

For ions, the mass fraction is defined as  $X_s = \rho_s/\rho$  and  $n_s = \rho_s/(A_s m_{\rm p})$ , so

$$\epsilon_{\text{diff}} = \mathbf{g} \cdot \sum_{\text{ions}} \mathbf{w}_s X_s \left( 1 - \frac{Z_s / A_s}{\langle Z_i \rangle / \langle A \rangle} \right).$$
 (B17)

This term only appears if the charge-to-mass ratio of the species being transported is different than the background. In the limit in which all other isotopes have  $Z_s/A_s=1/2$  and  $\langle Z_i \rangle/\langle A \rangle=1/2$  (trace limit), the only nonzero term is that for <sup>22</sup>Ne. That is,

$$\epsilon_{\text{diff}} = \epsilon_{22} = 2gw_{22}X_{22}/22,$$
 (B18)

which is equivalent to Equation (16) in Paxton et al. (2018).

### B.3. Demonstration of Equivalence

Alternatively, taking the sum over all species (including electrons) in Equation (B14), the gravitational and electric force terms vanish due to the lack of net flow of mass and charge. The term with the electron chemical potential gradient

remains, implying

$$\epsilon_{\text{diff}} = -\frac{n_e}{\rho} \mathbf{w}_e \cdot \nabla \mu_e = -\frac{\langle Z_i \rangle}{\langle A \rangle m_p} \mathbf{w}_e \cdot \nabla \mu_e. \tag{B19}$$

The constraints of no net transport of mass or charge also imply that the electron velocity is related to the ion velocity. In the context of two species, the mass constraint is

$$X_{22}\mathbf{w}_{22} + (1 - X_{22})\mathbf{w}_b = 0 (B20)$$

and the charge constraint is

$$\frac{\langle Z_{i} \rangle}{\langle A \rangle} w_{e} = X_{22} \frac{Z_{22}}{A_{22}} w_{22} + (1 - X_{22}) \frac{Z_{b}}{A_{b}} w_{b}.$$
 (B21)

Combining these, and assuming a background with  $Z_b/A_b = 1/2$ , we have

$$\frac{\langle Z_i \rangle}{\langle A \rangle} w_e = \left(\frac{10}{22} - \frac{Z_b}{A_b}\right) X_{22} w_{22} = -\frac{X_{22}}{22} w_{22}. \tag{B22}$$

This demonstrates that Equations (B12) and (B18) are equivalent.

This clarifies that the MESA approach retains only the local entropy generation term in Equation (B1) and shows why García-Berro et al. (2008) and MESA agree on the net effect of sedimentation on WD cooling despite the apparently different approaches.

# Appendix C Charge Stratification

In this section, we tentatively rule out any physical process that relies on stratification of elements by charge as a source of  $\sim\!10$  Gyr cooling delays. In strongly coupled Coulomb mixtures, ions of higher-than-average charge also sediment, even with equal charge-to-mass ratio (Chang et al. 2010; Beznogov & Yakovlev 2013). The forces associated with this tendency toward charge stratification can modify diffusion velocities of elements responsible for sedimentation heating, and movement of ions through the chemical potential gradient driving this charge separation yields an additional heating term (Equation (B14)). However, we show here that this term is small compared to single-particle  $^{22}$ Ne sedimentation heating in WD interiors.

Following Beznogov & Yakovlev (2013), for species j of charge  $Z_j$ , the Coulomb interactions with other ions give rise to a chemical potential of the form

$$\mu_j^{(C)} = -0.9 \frac{Z_j^{5/3} e^2}{a_e},$$
 (C1)

and therefore the average Coulomb chemical potential over all ions in the plasma is

$$\langle \mu^{(C)} \rangle = -0.9 \Gamma k_{\rm B} T. \tag{C2}$$

The charge separation force for element j relative to the background of all ions is then (see Equation (14) of Beznogov

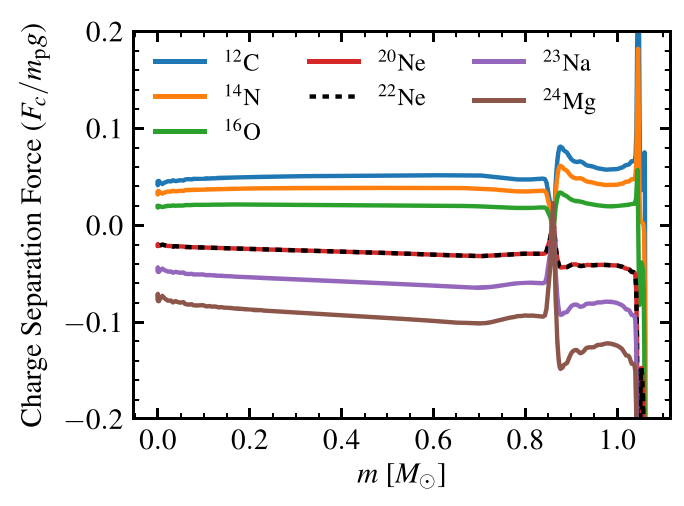


**Figure 14.** Example of the charge separation forces in a 1.06  $M_{\odot}$  O/Ne WD. This model has cooled to a luminosity of  $10^{-2}\,L_{\odot}$  and will soon begin core crystallization.

& Yakovlev 2013)

$$F_{c,j} \equiv \frac{1}{\langle Z_{i} \rangle} [Z_{j} \nabla \langle \mu^{(C)} \rangle - \langle Z_{i} \rangle \nabla \mu_{j}^{(C)}]$$

$$\approx \left( \frac{Z_{j}}{\langle Z_{i} \rangle} - \frac{Z_{j}^{5/3}}{\langle Z_{i}^{5/3} \rangle} \right) \nabla \langle \mu^{(C)} \rangle, \tag{C3}$$

where we have assumed that  $\nabla\langle Z_i^{5/3}\rangle$  is negligible for the final step. Figure 14 shows this estimated force relative to the local value of  $m_p g$  for each species of ion throughout the interior profile of a 1.06  $M_\odot$  MESA WD model with an O/Ne dominated core. While these forces may be enough to drive small amounts of diffusion, they are much smaller than the gravitational sedimentation forces ( $F_g \geqslant m_p g$ ) that act on neutron-rich isotopes such as <sup>22</sup>Ne and <sup>23</sup>Na. Diffusion velocities are linearly proportional to the forces driving them  $v \propto F$ , and heating associated with these velocities scales as  $\epsilon \propto vF \propto F^2$ . Diffusion related to charge separation will therefore lead to negligible heating compared to gravitational sedimentation, so we are justified in ignoring this term in the models presented in this work.

Figure 14 also allows an estimate of the total amount of energy that could be released associated with any other mixing that might lead to rearrangement of charges in this chemical potential (e.g., phase separation induced by crystallization) using Equation (5). For the most abundant elements (O and Ne in this MESA model), complete charge stratification would lead to a delay of approximately 5 Gyr. This is somewhat smaller than the energy and cooling delay available from <sup>22</sup>Ne sedimentation. The ratio of the total energies from both of these approximately  $E_g/E_c \approx (2X_{22})(F_g/F_c) \approx 200X_{22}$ . So the total time delay available from charge separation is comparable to that available from complete <sup>22</sup>Ne when metallicity is  $Z \approx 0.005$ , but WDs descended from metal-rich stars have a potential sedimentation energy reservoir several times larger.

We also note that this energy estimate predicts that cooling delays comparable to those observed for the Q branch could only result from phase separation if chemical separation of the dominant elements (C/O or O/Ne) is nearly complete,

releasing all of the energy associated with these chemical potential differences. In fact, phase separation calculations do not predict complete separation, and hence cooling delays associated with phase separation are typically on the order of 1 Gyr (Segretain et al. 1994; Chabrier et al. 2000; Althaus et al. 2012), insufficient to explain the full extent of the cooling anomaly on the *Q* branch.

### **ORCID iDs**

```
References
Althaus, L. G., Córsico, A. H., Bischoff-Kim, A., et al. 2010a, ApJ, 717, 897
Althaus, L. G., Córsico, A. H., Isern, J., & García-Berro, E. 2010b, A&ARv,
  18, 471
Althaus, L. G., García-Berro, E., Isern, J., Córsico, A. H., &
  Miller Bertolami, M. M. 2012, A&A, 537, A33
Althaus, L. G., García-Berro, E., Renedo, I., et al. 2010c, ApJ, 719, 612
Bedin, L. R., King, I. R., Anderson, J., et al. 2008, ApJ, 678, 1279
Bergeron, P., Dufour, P., Fontaine, G., et al. 2019, ApJ, 876, 67
Bergeron, P., Wesemael, F., Dufour, P., et al. 2011, ApJ, 737, 28
Beznogov, M. V., & Yakovlev, D. G. 2013, PhRvL, 111, 161101
Bildsten, L., & Hall, D. M. 2001, ApJL, 549, L219
Blouin, S., Daligault, J., Saumon, D., Bédard, A., & Brassard, P. 2020, A&A,
  640, L11
Blouin, S., Dufour, P., & Allard, N. F. 2018, ApJ, 863, 184
Brooks, J., Schwab, J., Bildsten, L., Quataert, E., & Paxton, B. 2017, ApJL,
  834, L9
Burgers, J. M. 1969, Flow Equations for Composite Gases (New York:
  Academic)
Camisassa, M. E., Althaus, L. G., Córsico, A. H., et al. 2019, A&A, 625, A87
Campos, F., Bergeron, P., Romero, A. D., et al. 2016, MNRAS, 456, 3729
Castro, S., Rich, R. M., Grenon, M., Barbuy, B., & McCarthy, J. K. 1997, AJ,
Chabrier, G., Brassard, P., Fontaine, G., & Saumon, D. 2000, ApJ, 543, 216
Chang, P., Bildsten, L., & Arras, P. 2010, ApJ, 723, 719
Cheng, S., Cummings, J. D., & Ménard, B. 2019, ApJ, 886, 100
Cheng, S., Cummings, J. D., Ménard, B., & Toonen, S. 2020, ApJ, 891, 160
Clayton, G. C., Geballe, T. R., Herwig, F., Fryer, C., & Asplund, M. 2007,
   ApJ, 662, 1220
Cooper, R. L., & Bildsten, L. 2008, PhRvE, 77, 056405
Coutu, S., Dufour, P., Bergeron, P., et al. 2019, ApJ, 885, 74
Daligault, J. 2006a, PhRvL, 96, 065003
Daligault, J. 2006b, PhRvE, 73, 056407
de Groot, S. R., & Mazur, P. 1969, Non-Equilibrium Thermodynamics (Berlin:
  Springer-Verlag)
Deloye, C. J., & Bildsten, L. 2002, ApJ, 580, 1077
Donkó, Z., Kalman, G. J., & Golden, K. I. 2002, PhRvL, 88, 225001
Dunlap, B. H., & Clemens, J. C. 2015, in ASP Conf. Ser. 493, 19th European
   Workshop on White Dwarfs, ed. P. Dufour, P. Bergeron, & G. Fontaine
  (San Francisco, CA: ASP), 547
Fontaine, G., Brassard, P., & Bergeron, P. 2001, PASP, 113, 409
Gaia Collaboration, Babusiaux, C., van Leeuwen, F., et al. 2018a, A&A,
  616, A10
Gaia Collaboration, Brown, A. G. A., Vallenari, A., et al. 2018b, A&A,
  616, A1
Gaia Collaboration, Prusti, T., de Bruijne, J. H. J., et al. 2016, A&A, 595, A1
García-Berro, E., Althaus, L. G., Córsico, A. H., & Isern, J. 2008, ApJ,
```

García-Berro, E., Torres, S., Althaus, L. R. G., et al. 2010, Natur, 465, 194

Gentile Fusillo, N. P., Tremblay, P.-E., Gänsicke, B. T., et al. 2019, MNRAS,

Hansen, B. M. S., Brewer, J., Fahlman, G. G., et al. 2002, ApJL, 574, L155 Hayden, M. R., Bovy, J., Holtzman, J. A., et al. 2015, ApJ, 808, 132

Hirschfelder, J. O., Curtiss, C. F., & Bird, R. B. 1964, Molecular Theory of

Hansen, B. M. S., Anderson, J., Brewer, J., et al. 2007, ApJ, 671, 380

Gases and Liquids (New York: Wiley)

Holberg, J. B., & Bergeron, P. 2006, AJ, 132, 1221

677, 473

```
Horowitz, C. J., Schneider, A. S., & Berry, D. K. 2010, PhRvL, 104, 231101
Hughto, J., Horowitz, C. J., Schneider, A. S., et al. 2012, PhRvE, 86, 066413
Hughto, J., Schneider, A. S., Horowitz, C. J., & Berry, D. K. 2010, PhRvE, 82,
Hunter, J. D. 2007, CSE, 9, 90
Isern, J., Hernanz, M., Mochkovitch, R., & Garcia-Berro, E. 1991, A&A,
   241, L29
Jeffery, C. S., Karakas, A. I., & Saio, H. 2011, MNRAS, 414, 3599
Khoperskov, S., Di Matteo, P., Haywood, M., Gómez, A., & Snaith, O. N.
   2020, A&A, 638, A144
Kilic, M., Bergeron, P., Kosakowski, A., et al. 2020, ApJ, 898, 84
Kippenhahn, R., Thomas, H. C., & Weigert, A. 1965, ZA, 61, 241
Kippenhahn, R., Weigert, A., & Weiss, A. 2012, Stellar Structure and
   Evolution (Berlin: Springer-Verlag)
Kluyver, T., Ragan-Kelley, B., Pérez, F., et al. 2016, in Positioning and Power
   in Academic Publishing: Players, Agents and Agendas: Proc. 20th Int. Conf.
   on Electronic Publishing 87 (Amsterdam: IOS Press),
Koester, D. 2010, MmSAI, 81, 921
Koester, D., & Kepler, S. O. 2019, A&A, 628, A102
Lamb, D. Q., & van Horn, H. M. 1975, ApJ, 200, 306
Lauffer, G. R., Romero, A. D., & Kepler, S. O. 2018, MNRAS, 480, 1547
Mackereth, J. T., Bovy, J., Leung, H. W., et al. 2019, MNRAS, 489, 176
McCleery, J., Tremblay, P.-E., Fusillo, N. P. G., et al. 2020, MNRAS, in press
   (doi:10.1093/mnras/staa2030)
McKeever, J. M., Basu, S., & Corsaro, E. 2019, ApJ, 874, 180
Medin, Z., & Cumming, A. 2010, PhRvE, 81, 036107
Medin, Z., & Cumming, A. 2011, ApJ, 730, 97
```

Mestel, L. 1952, MNRAS, 112, 583

```
Mochkovitch, R. 1983, A&A, 122, 212
Nidever, D. L., Bovy, J., Bird, J. C., et al. 2014, ApJ, 796, 38
Paxton, B., Bildsten, L., Dotter, A., et al. 2011, ApJS, 192, 3
Paxton, B., Cantiello, M., Arras, P., et al. 2013, ApJS, 208, 4
Paxton, B., Marchant, P., Schwab, J., et al. 2015, ApJS, 220, 15
Paxton, B., Schwab, J., Bauer, E. B., et al. 2018, ApJS, 234, 34
Paxton, B., Smolec, R., Schwab, J., et al. 2019, ApJS, 243, 10
Pérez, F., & Granger, B. E. 2007, CSE, 9, 21
Pompéia, L., Barbuy, B., & Grenon, M. 2003, ApJ, 592, 1173
Potekhin, A. Y., & Chabrier, G. 2010, CoPP, 50, 82
Rohrmann, R. D., Althaus, L. G., García-Berro, E., Córsico, A. H., &
  Miller Bertolami, M. M. 2012, A&A, 546, A119
Romero, A. D., Kepler, S. O., Córsico, A. H., Althaus, L. G., & Fraga, L. 2013,
  ApJ, 779, 58
Segretain, L., & Chabrier, G. 1993, A&A, 271, L13
Segretain, L., Chabrier, G., Hernanz, M., et al. 1994, ApJ, 434, 641
Sharma, S., Hayden, M. R., & Bland-Hawthorn, J. 2020, arXiv:2005.03646
Siess, L. 2006, A&A, 448, 717
Siess, L. 2007, A&A, 476, 893
Staff, J. E., Menon, A., Herwig, F., et al. 2012, ApJ, 757, 76
Stanton, L. G., & Murillo, M. S. 2016, PhRvE, 93, 043203
Temmink, K. D., Toonen, S., Zapartas, E., Justham, S., & Gänsicke, B. T.
  2020, A&A, 636, A31
Towns, J., Cockerill, T., Dahan, M., et al. 2014, CSE, 16, 62
Tremblay, P.-E., Fontaine, G., Fusillo, N. P. G., et al. 2019, Natur, 565, 202
van der Walt, S., Colbert, S. C., & Varoquaux, G. 2011, CSE, 13, 22
van Horn, H. M. 1968, ApJ, 151, 227
```